8

Unusually High Thermal Conductivity in Carbon Nanotubes

Young-Kyun Kwon and Philip Kim

Recently discovered carbon nanotubes have exhibited many unique material properties including very high thermal conductivity. Strong sp^2 bonding configurations in carbon network and nearly perfect self-supporting atomic structure in nanotubes give unusually high phonon-dominated thermal conductivity along the tube axis, possibly even surpassing that of other carbon-based materials such as diamond and graphite (in plane). In this chapter, we explore theoretical and experimental investigations for the thermal-transport properties of these materials.

8.1 Introduction

The miniaturization of electrical and mechanical systems is the main achievement of modern technology, making faster and more efficient devices. With the continually decreasing size of electronic devices and microelectromechanical systems (MEMS), there is an increasing effort to use nanoscale materials as components of nanoscale devices. The thermal properties of the nanoscale materials are of fundamental interest and play a critical role in controlling the performance and stability of the device that consists of these materials. Among these materials, carbon nanotubes are of particular interest for their unique electric and thermal properties [1], [2].

Carbon nanotubes were discovered by Iijima in 1991 [3]. These novel materials, in fact, are natural extensions of fullerene clusters that have been extensively studied since the discovery of C_{60} [4] in 1985. Like other fullerenes, carbon nanotubes are made of only carbon, and the sp^2 bonding yields a π-bonding network. However, unlike most fullerenes and their derivatives, carbon nanotubes have extremely high aspect ratios. Structurally, carbon nanotubes consist of seamless cylindrical tubes that can be conceptually formed by cutting and rolling up a graphene sheet (a single layer of graphite). Single-walled nanotubes (SWNTs) consist of only a single seamless cylinder, whereas multiwalled nanotubes (MWNTs) consist of several concentric shells.

Traditionally, carbon-based materials, such as diamond and graphite, have been a material class that exhibits very high thermal conductivity. Isotope

impurity-free monocrystalline diamond is one of the best thermal conductors due to the high speed of sound resulting from the stiff covalent sp^3 bonds between the carbon atoms and greatly suppressed impurity phonon scattering [5]. High thermal conductivity should also be expected in carbon nanotubes, which are held together by even stronger sp^2 bonds. These systems, consisting of seamless and atomically perfect graphitic cylinders a few nanometers in diameter, are self-supporting. Thus, the rigidity of the graphitic walls, combined with the absence of atomic defects or coupling to soft phonon modes of the embedding medium, should make isolated nanotubes very good candidates for efficient thermal conductors.

In this chapter, we present both theoretical and experimental surveys for the investigation of thermal conduction in carbon nanotubes. In the first part, we present theoretical calculations of thermal conductivity of nanotubes. After a brief discussion of phonons in carbon nanotubes, we discuss several computational methods based on molecular dynamics simulations used to determine thermal conductivity of nanotubes. The resulting thermal conductivities of carbon nanotubes and other carbon allotropes and their temperature dependencies will be reviewed. An unusually high thermal conductivity is predicted for isolated SWNTs in the calculations. In the second part, we discuss the reported experimental results in thermal-conductivity measurements of carbon nanotube materials. First, the bulk measurements including carbon nanotube composite materials are reviewed. In addition, a detailed description of recently demonstrated mesoscopic nanotube thermal-transport measurement will be presented. Finally, the comparison of theoretical and experimental results is given in the last part of the chapter, which confirms the proposed unusually high thermal conductivity in these materials.

8.2 Theory of Energy Conduction in Carbon Nanotubes

The thermal-transport properties of materials can be calculated using two main computational schemes. One scheme is the use of the Boltzmann equation, and the other is based on linear response theory from which the thermal correlation functions are derived. Whereas the former scheme, which is empirical, can be applied only to the materials that have experimental inputs available, the latter, which can be performed from first principle, is often used to predict the thermal properties of newly synthesized materials such as carbon nanotubes.

Carbon nanotubes are classified primarily into achiral and chiral nanotubes [1], [6]. An achiral nanotube exhibits a mirror symmetry on the plane normal to the tube axis whereas a chiral one shows a spiral symmetry. There are only two types of achiral nanotubes that show higher symmetry than chiral tubes. One is an "armchair" type and the other a "zigzag," as discussed later. The structure of a nanotube is more specified by the orientation of hexagonal carbon rings on cylindrical graphene sheets with respect to the tube axis.

This orientation is characterized by the chiral index (n, m) defined by the chiral vector $\mathbf{C}_h$

$$\mathbf{C}_h = n\mathbf{a}_1 + m\mathbf{a}_2, \tag{8.1}$$

where $\mathbf{a}_i (i = 1, 2)$ are real space unit vectors of the hexagonal lattice. This chiral vector, as shown in Fig. 8.1, connects two equivalent sites O and A on a graphene sheet. Its magnitude $\boldsymbol{C}_h$ represents a circumferential length of a nanotube being characterized by $\mathbf{C}_h$. The direction perpendicular to $\mathbf{C}_h$ becomes a tube axis. A pair of integers (n, m) in Eq. (8.1), specifying all possible chiral vectors, defines a different way of rolling the graphene sheet to form a nanotube. Zigzag nanotubes, which have the zigzag shape of the cross-sectional ring, and armchair nanotubes, which have the armchair shape, are denoted by the vectors $(n, 0)$ and (n, n), respectively.

The tube diameter d_t is given by

$$\begin{aligned} d_t &= \boldsymbol{C}_h/\pi \\ &= \sqrt{3} d_{CC}(n^2 + nm + m^2)^{1/2}/\pi, \end{aligned} \tag{8.2}$$

where d_{CC} is the nearest-neighbor distance between two carbon atoms (in graphite $d_{CC} = 1.42$Å). And the chiral angle θ, defined as the angle between the chiral vector $\mathbf{C}_h$ and the lattice vector $\mathbf{a}_1$, is given by

$$\begin{aligned} \cos\theta &= \frac{\boldsymbol{C}_h \cdot \mathbf{a}_1}{\boldsymbol{C}_h a} \\ &= \frac{2n + m}{2\sqrt{n^2 + nm + m^2}}. \end{aligned} \tag{8.3}$$

The chiral angle θ is just in the range of $0 \le |\theta| \le 30°$, because of the hexagonal symmetry of the graphene sheet. Armchair nanotubes, in particular, correspond to $\theta = 30°$ and zigzag ones $\theta = 0°$.

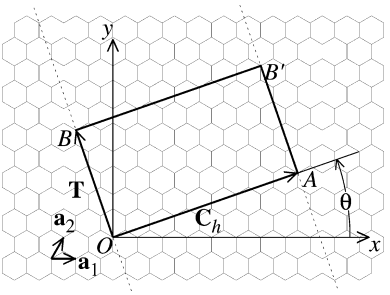

Fig. 8.1. A nanotube can be constructed by connecting site O to site A and site B to site B'. This nanotube is $(6, 3)$ (see the text for the tube classification). The chiral vector $\mathbf{C}_h$ and the translational vector $\mathbf{T}$ of the nanotube are represented by arrow lines of OA and OB, respectively. The rectangle $OAB'B$ defines the unit cell of the nanotube.

The vector $\mathbf{T}$, called the translation vector, is parallel to the tube axis, that is, perpendicular to the chiral vector $\mathbf{C}_h$. Using the relation of $\mathbf{C}_h \cdot \mathbf{T} = 0$, the vector $\mathbf{T}$, which becomes the lattice vector in a 1D tube unit cell, can be expressed in terms of the basis vectors $\mathbf{a}_i$ as

$$\mathbf{T} = \frac{1}{d_R}[-(n+2m)\mathbf{a}_1 + (2n+m)\mathbf{a}_2], \tag{8.4}$$

where d_R is the greatest common divisor of $(n+2m)$ and $(2n+m)$. Furthermore, d_R can be expressed in terms of the greatest common divisor d of n and m. If $n-m$ is a multiple of $3d$, $d_R = 3d$; otherwise $d_R = d$. Note that the bigger d_R, the smaller the length of $\mathbf{T}$. For example, $\mathbf{T} = -\mathbf{a}_1 + \mathbf{a}_2$ for any (n,n) armchair nanotubes ($d_R = 3d = 3n$) and $\mathbf{T} = -\mathbf{a}_1 + 2\mathbf{a}_2$ for any $(n,0)$ zigzag nanotubes ($d_R = n$). A $(6,3)$ nanotube ($d = d_R = 3$) shown in Fig. 8.1 has $\mathbf{T} = -4\mathbf{a}_1 + 5\mathbf{a}_2$.

The rectangle formed by two vectors $\mathbf{C}_h$ and $\mathbf{T}$ determines the unit cell of a nanotube, as shown as $OAB'B$ in Fig. 8.1. Because, in this unit cell there are $2N$ carbon atoms (the number of hexagons N in the unit cell is expressed in terms of n, m, and d_R as $N = 2(n^2 + nm + m^2)/d_R$) we expect there are $6N$ phonon-dispersion branches.

The corresponding vectors in reciprocal space are determined from the relations

$$\begin{aligned} \mathbf{C}_h \cdot \mathbf{K}_1 &= 2\pi, \quad & \mathbf{T} \cdot \mathbf{K}_1 &= 0, \\ \mathbf{C}_h \cdot \mathbf{K}_2 &= 0, \quad & \mathbf{T} \cdot \mathbf{K}_2 &= 2\pi, \end{aligned} \tag{8.5}$$

where $\mathbf{K}_1$ is in the circumferential direction and $\mathbf{K}_2$ along the tube axis. The resulting expressions for $\mathbf{K}_1$ and $\mathbf{K}_2$ are given by

$$\begin{aligned} \mathbf{K}_1 &= \frac{1}{N}(-t_2\mathbf{b}_1 + t_1\mathbf{b}_2), \\ \mathbf{K}_2 &= \frac{1}{N}(m\mathbf{b}_1 - n\mathbf{b}_2), \end{aligned} \tag{8.6}$$

where $\mathbf{b}_i$ $(i = 1, 2)$ are the reciprocal lattice vectors of the hexagonal lattice. $\mathbf{K}_2$ is the *reciprocal lattice vector* that is the counterpart of $\mathbf{T}$ in real space, whereas $\mathbf{K}_1$ is just a corresponding vector to $\mathbf{C}_h$, which gives discrete k values in the circumferential direction.

In this section, we discuss the computational approach to probe the thermal properties of carbon nanotubes. After we review phonon-dispersion relations of 2-dimensional (2D) graphite and carbon nanotubes, we describe computational methods based on molecular dynamics simulations for determining thermal conductivity and their pitfalls when applied to nanotubes. Combining equilibrium and nonequilibrium molecular dynamics simulations with Green-Kubo formalism, we determine the thermal conductivity of SWNTs and other carbon allotropes. Our results suggest an unusually high value $\kappa \approx 6,600\,\mathrm{W/m \cdot K}$ for an isolated $(10,10)$ nanotube at room temperature, comparable to the thermal conductivity of a hypothetical isolated

graphite monolayer or diamond. We find that these high values of κ are associated with large phonon mean free paths in these systems.

8.2.1 Phonons in Carbon Nanotubes

It has been shown that the 1-dimensional (1D) electronic band structure of carbon nanotubes [7], [8], [9] can be obtained from that of an ideal 2D graphene sheet using the zone-folding approach. Likewise, the zone-folding approach has been used to determine the phonon-dispersion relations of carbon nanotubes from those of the graphene sheet [6], [10], [11], obtained by solving the secular equation of its dynamical matrix to be determined by a simple force constant model. (See [6], [11] for a more detailed description of phonon modes of 2D graphite and carbon nanotubes.)

The equations of motion of the lattice are, in general, expressed as

$$m_i \ddot{\mathbf{x}}_i = -\sum_j K^{(ij)}(\mathbf{x}_i - \mathbf{x}_j)\,, \quad (i = 1, \ldots, N), \tag{8.7}$$

where m_i and $\mathbf{x}_i$ are, respectively, the mass and the displacement vector from its equilibrium position of the ith atom among N atoms in a unit cell, and $K^{(ij)}$ is the 3×3 force constant matrix between the ith and jth atoms. $\sum_j$ means the summation taken over all interacting neighbor atoms, which are usually considered up to the nth nearest neighbors, including ones in other unit cells. If we seek normal mode solutions of Eq. (8.7)

$$\mathbf{x}_l = \sum_{\mathbf{k}} \mathbf{u}_{\mathbf{k}}^{(l)} e^{-i(\mathbf{k}\cdot\mathbf{r}_l - \omega t)}, \tag{8.8}$$

where the summation is taken over all the wave vectors $\mathbf{k}$ in the first Brillouin zone. Here $\mathbf{r}_l$ is the equilibrium position of the lth atom and $\mathbf{u}_{\mathbf{k}}^{(l)}$ denotes the Fourier coefficient of $\mathbf{x}_l$. We assume the same eigenfrequencies ω for all $\mathbf{x}_l$. Substituting Eq. (8.8) into Eq. (8.7) and using the orthogonal condition in reciprocal space,

$$\sum_{\mathbf{r}_l} e^{-i(\mathbf{k}-\mathbf{k}')\cdot\mathbf{r}_l} = \delta(\mathbf{k} - \mathbf{k}'), \tag{8.9}$$

where $\delta(\mathbf{k} - \mathbf{k}')$ is a delta function in the continuum k space, Eq. (8.7) becomes

$$-m_i\omega^2 I \mathbf{u}_{\mathbf{k}}^{(i)} = -\sum_j K^{(ij)} \left(\mathbf{u}_{\mathbf{k}}^{(i)} - e^{-i\mathbf{k}\cdot\mathbf{r}_{ij}} \mathbf{u}_{\mathbf{k}}^{(j)}\right), \quad (i = 1, \ldots, N), \tag{8.10}$$

where $\mathbf{r}_{ij} = \mathbf{r}_i - \mathbf{r}_j$ and I is a 3×3 identity matrix. This equation can be written more compactly in a tensor form as

$$\mathcal{D}(\mathbf{k})\mathbf{u}_{\mathbf{k}} = 0, \tag{8.11}$$

where $\mathcal{D}(\mathbf{k})$ is a $3N \times 3N$ matrix called a dynamical matrix and decomposed into the total N^2 number of 3×3 submatrices $\{\mathcal{D}^{(ij)}(\mathbf{k})\}$ expressed as

$$\mathcal{D}^{(ij)}(\mathbf{k}) = \left(\sum_l K^{(il)} - m_i \omega^2(\mathbf{k}) I \right) \delta_{ij} - K^{(ij)} e^{i\mathbf{k}\cdot\mathbf{r}_{ij}}. \tag{8.12}$$

Note that the dynamical matrix includes the contributions from all interacting neighbor atoms. Equation (8.11) is simply an eigenvalue equation, whose nontrivial solutions are obtained by finding the eigenvalues $\omega^2(\mathbf{k})$ resulting when the secular equation $\det \mathcal{D}(\mathbf{k}) = 0$ is solved for a given $\mathbf{k}$ vector.

For a single graphene sheet, in the unit cell of which there are two carbon atoms, α and β, its dynamical matrix will be a 6×6 matrix and can be expressed as

$$\begin{pmatrix} \mathcal{D}^{(\alpha\alpha)} & \mathcal{D}^{(\alpha\beta)} \\ \mathcal{D}^{(\beta\alpha)} & \mathcal{D}^{(\beta\beta)} \end{pmatrix} \tag{8.13}$$

in terms of the 3×3 submatrices $\mathcal{D}^{(ij)}$, $(i, j = \alpha, \beta)$. $\mathcal{D}^{(ij)}$ contains all the contributions to the atom i from up to the fourth nearest-neighbor atoms equivalent to the atom j. As given in Eq. (8.12), $\mathcal{D}^{(ij)}$ is constructed by calculating the force constant matrix $K^{(ij)}$, which is composed of the force constant parameters $f_r^{(n)}$, $f_{t_i}^{(n)}$, and $f_{t_o}^{(n)}$, $(n = 1, \ldots, 4)$, which are determined by the interactions of the nth neighbor atoms, in the radial (bond stretching), in-plane and out-of-plane tangential (bond-bending) directions, respectively. Table 8.1, which was originally shown in [10], gives values for the force constant parameters for 2D graphite obtained by fitting to experimental phonon-dispersion relations measured along the ΓM direction [12], [13].

Consider the contributions to the atom α from three first nearest neighbor atoms $\beta_1^{(1)}$, $\beta_2^{(1)}$, and $\beta_3^{(1)}$. Assume that the atom $\beta_1^{(1)}$ is in the same unit cell as the atom α, whereas each of the other two atoms is in a neighboring unit cell. In a coordinate system in which the atom α is at the origin, the atom β_1 is on the x-axis, and the z-axis perpendicular to the graphene sheet is passing by the atom α. Then, the contribution from the atom $\beta_1^{(1)}$ to the

Table 8.1. Values for the force constant parameters $f_r^{(n)}$, $f_{t_i}^{(n)}$, and $f_{t_o}^{(n)}$ $(n = 1, \ldots, 4)$, for 2D graphite up to the $n =$ fourth nearest neighbor interactions, originally shown in [10]. The subscripts r, t_i, and t_o refer to radial, tangential in plane, and out of plane, respectively. The values are given in units of 10^4 dyn/cm.

Radial	Tangential	
$f_r^{(1)} = 36.50$	$f_{t_i}^{(1)} = 24.50$	$f_{t_o}^{(1)} = 9.82$
$f_r^{(2)} = 8.80$	$f_{t_i}^{(2)} = -3.23$	$f_{t_o}^{(2)} = -0.40$
$f_r^{(3)} = 3.00$	$f_{t_i}^{(3)} = -5.25$	$f_{t_o}^{(3)} = 0.15$
$f_r^{(4)} = -1.92$	$f_{t_i}^{(4)} = 2.29$	$f_{t_o}^{(4)} = -0.58$

force constant matrix $K^{(\alpha\beta)}$ is given by

$$\tilde{K}\left(\alpha\beta_1^{(1)}\right) = \begin{pmatrix} f_r^{(1)} & 0 & 0 \\ 0 & f_{t_i}^{(1)} & 0 \\ 0 & 0 & f_{t_o}^{(1)} \end{pmatrix}. \tag{8.14}$$

The force constant matrix K is expressed in terms of $\tilde{K}$ as

$$K^{(\alpha\beta)} \equiv \sum_n \sum_l \tilde{K}\left(\alpha\beta_l^{(n)}\right). \tag{8.15}$$

Using a rotation matrix R_l given by

$$R_l = \begin{pmatrix} \cos\phi_l & \sin\phi_l & 0 \\ -\sin\phi_l & \cos\phi_l & 0 \\ 0 & 0 & 1 \end{pmatrix}, \quad (l = 2, 3), \tag{8.16}$$

where $\phi_l = 2(l-1)\pi/3$ are rotational angles between $\beta_1^{(1)}$ and $\beta_l^{(1)}$, the contributions from the other two atoms $\beta_2^{(1)}$ and $\beta_3^{(1)}$, both of which are geometrically equivalent to the atom $\beta_1^{(1)}$, are expressed by

$$\tilde{K}\left(\alpha\beta_l^{(1)}\right) = R_l^{-1}\tilde{K}\left(\alpha\beta_1^{(1)}\right)R_l, \quad (l = 2, 3). \tag{8.17}$$

We also calculate all other contributions of the nth nearest neighbor atoms to the force constant matrix in a similar way. Considering all these contributions and the corresponding phase factor $e^{i\mathbf{k}\cdot\mathbf{r}_{ij}}$, we complete the construction of the dynamical matrix $\mathcal{D}(\mathbf{k})$ and thus obtain the phonon-dispersion relations by solving the secular equation $\det \mathcal{D}(\mathbf{k}) = 0$.

The phonon-dispersion relations for 2D graphite are displayed in Fig. 8.2. There are a total of six phonon branches, three of which correspond to acoustic modes that have zero energy at the Γ point, and the other three are optical. The lowest mode in energy corresponds to the t_o mode, and the second and third lowest ones to t_i and r, respectively, near the Γ point. The t_i and r modes, both of which are *in-plane* modes, show a linear k dependence as usually seen for acoustic modes, whereas the t_o mode that is an *out-of-plane* mode, shows a special k^2 dependence, which comes from the three-fold rotational symmetry (C_3) around the z-axis. Although no linear combination of k_x and k_y can be invariant under C_3 rotation, the quadratic form of $k_x^2 + k_y^2$ as well as a constant is invariant. Similarly, the optical t_o mode ($\omega \sim 865\,\mathrm{cm}^{-1}$ at $k = 0$) shows a k^2 dependence.

The phonon-dispersion relations for SWNTs are obtained by the zone-folding method from those of 2D graphite $\omega_{\mathrm{gra}}^l(\mathbf{k})$ (see Fig. 8.2), where $l = 1, \ldots, 6$ labels six phonon branches and $\mathbf{k}$ is a vector in 2D reciprocal space. Supposed that an SWNT has N hexagons in its unit cell, that is, $2N$ carbon

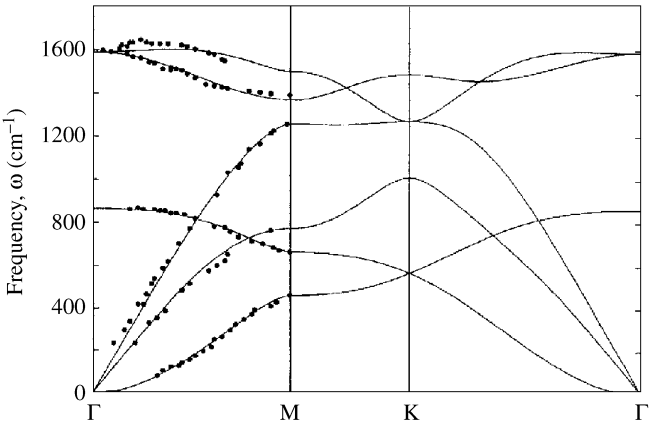

Fig. 8.2. The phonon-dispersion relations for the 2D graphene sheet, plotted along high-symmetry directions, using the set of the force constant parameters in Table 8.1 [10], [11]. The points shown along the ΓM line are experimental values [12], [13]. [Courtesy of Millie Dresselhaus]

atoms. Then its phonon-dispersion relations $\omega_{\rm nt}^{l\nu}(k)$ are given in terms of $\mathbf{K}_i$, $(i = 1, 2)$ given in Eq. (8.6) by

$$\omega_{\rm nt}^{l\nu}(k) = \omega_{\rm gra}^{l}\left(\nu\mathbf{K}_1 + k\frac{\mathbf{K}_2}{|\mathbf{K}_2|}\right), \tag{8.18}$$

where $\nu = 0, \ldots, N-1$ and k is a 1D wave vector of the nanotube ranging from $-\pi/T$ to π/T with $T = |\mathbf{T}|$.

Although the zone-folding method describes the overall features of the phonon modes of a nanotube quite well, some of their features, especially near the low-frequency region, are not described by the method. For example, the acoustic t_o mode of 2D graphite, which has $\omega = 0$ at $\mathbf{k} = 0$, corresponds to a radial breathing mode in the carbon nanotube, which has *nonzero* frequency, $\omega > 0$, at the Γ point. Another example is an acoustic mode of a nanotube, the vibration of which is normal to the nanotube axis corresponding a rigid shift of the nanotube along, for example, the x-axis. This mode is formed by a linear combination of in-plane and out-of-plane modes in 2D graphite in which one mode is not coupled with the other. Hence, this mode is a unique acoustic mode of the nanotube.

To avoid considering these additional physical concepts to determine the phonon-dispersion relations of nanotubes, we solve the $6N \times 6N$ dynamical matrix $\mathcal{D}(\mathbf{k})$ of a nanotube, which has $2N$ carbon atoms denoted by α_i and β_j $(i, j = 1, \ldots, N)$, directly. (N atoms of α_i, (or β_j) are geometrically equivalent to each other.) Similarly as discussed earlier $\mathcal{D}$ is decomposed into 3×3 small

matrices $\mathcal{D}^{(\alpha_i\beta_j)}$ for a pair of α_i and β_j atoms as

$$\mathcal{D} = \begin{pmatrix} \ddots & & & \\ & \mathcal{D}^{(\alpha_i\alpha_j)} & \cdots & \mathcal{D}^{(\alpha_i\beta_j)} \\ & \vdots & \ddots & \vdots \\ & \mathcal{D}^{(\beta_i\alpha_j)} & \cdots & \mathcal{D}^{(\beta_i\beta_j)} \\ & & & \ddots \end{pmatrix}. \tag{8.19}$$

By a similar discussion on unitary transformation (see (8.14)–(8.17)), a contribution of the force constant matrix, $\tilde{K}^{(\alpha_i\beta_j^{(n)})}$ is calculated in terms of the nonzero contribution of the force constant matrix related to α_1 or β_1, using, for example,

$$\tilde{K}^{\left(\alpha_i\beta_j^{(n)}\right)} = R_{i-1}^{-1}\tilde{K}^{\left(\alpha_1\beta_{j-i+1}^{(n)}\right)}R_{i-1}, \tag{8.20}$$

where R_l is a unitary matrix for rotation by an angle $\phi = 2l\pi/N$ around the tube axis and given by Eq. (8.16) if the z-axis is taken for the tube axis. $\tilde{K}^{(\alpha_1\beta_1^{(1)})}$, in which $\beta_1^{(1)}$ is a nearest neighbor atom of the atom α_1 that is on the x-axis, is determined by rotating the matrix of Eq. (8.14) by an angle $\pi/6 - \theta$ around the x-axis, and then by an angle $\xi/2$ around the z-axis. Here, θ is the chiral angle of the tube and ξ is the angle between α_1 and $\beta_1^{(1)}$ around the z-axis. Once $\tilde{K}^{(\alpha_1\beta_1^{(1)})}$ is determined, all other contributions to the force constant matrices $\tilde{K}^{(\alpha_i\beta_j^{(1)})}$, $(i, j = 1, \ldots, N)$ of the nearest atoms β_j are obtained using Eq. (8.20). Similarly, the other contributions from nth nearest neighbor atoms are also determined, as are all of the force-constant matrices. The force-constant tensor along with the corresponding phase factor $e^{ikz_{ij}}$, where z_{ij} is the z-component of $\mathbf{r}_{ij}$, determines the dynamical matrix $\mathcal{D}$ to be solved for the phonon-dispersion relations of the nanotube. (For a more detailed description of the dynamical matrix $\mathcal{D}$ and consideration of curvature effects on the force-constant parameters, see [6]).

For example, the phonon-dispersion relations for a $(10, 10)$ carbon nanotube, which has $2N = 40$ carbon atoms in its unit cell, are displayed in Fig. 8.3. For 40 atoms, there should be 120 $(=3 \times 2N)$ vibrational degrees of freedom, but they exhibit only 66 distinct phonon modes, because 54 phonon branches are doubly degenerate and 12 modes are nondegenerate. The corresponding density of states (DOS) for a $(10, 10)$ nanotube is shown in Fig. 8.4, where, for comparison, that for a 2D graphene sheet is also shown with the same units of state/(C atom)/cm^{-1} scaled by a factor. The overall feature for the nanotube is similar to that for the graphene, because the phonon-dispersion relations of the former are related to the zone-folding of the latter. The differences between their detailed features originate from the van Hove singularities existing only in 1D nanotubes and the low-energy modes near the Γ point, as discussed later.

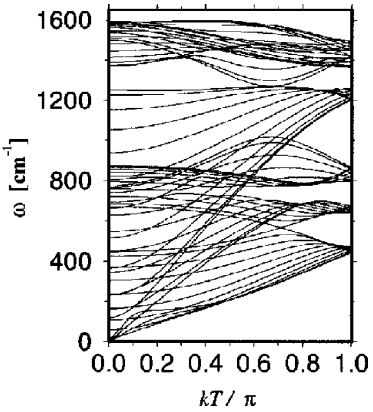

Fig. 8.3. The phonon-dispersion relations for a $(10, 10)$ carbon nanotube [11]. There are $2N = 40$ carbon atoms in its unit cell, thus 120 vibrational degrees of freedom, but there are only 66 distinct phonon modes because of degeneracies. The wave vector k is given in units of π/T. [Courtesy of Millie Dresselhaus]

Now, we consider the low-energy phonon modes near the Γ point. Shown in Fig. 8.5 are four acoustic branches, that have zero energy ($\omega = 0$) at the Γ point ($k = 0$), showing a linear k dependence. The transverse acoustic modes, which are doubly degenerated at the lowest energy curve, result from the vibrations (along the x- or y-direction) perpendicular to the tube axis. These modes do not exist in 2D graphite, as discussed earlier. The longitudinal acoustic mode or the vibration in the direction of the tube axis (z-axis) is shown as the highest energy acoustic mode in Fig. 8.5. The other acoustic phonon curve, located between the lowest and highest ones in Fig. 8.5,

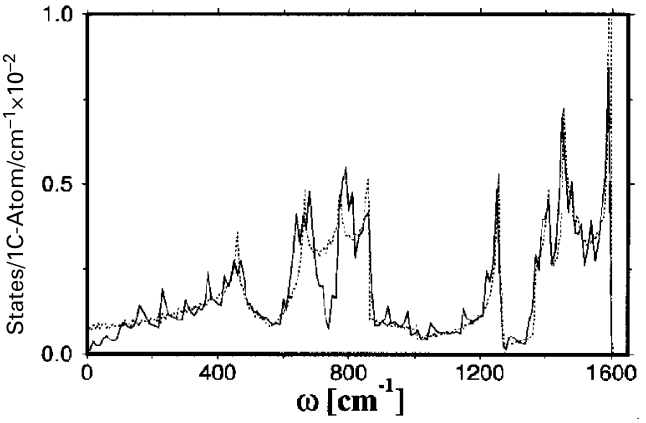

Fig. 8.4. The phonon densities of states for a $(10, 10)$ carbon nanotube (solid line) and a graphene sheet (dotted line) [11]. [Courtesy of Millie Dresselhaus]

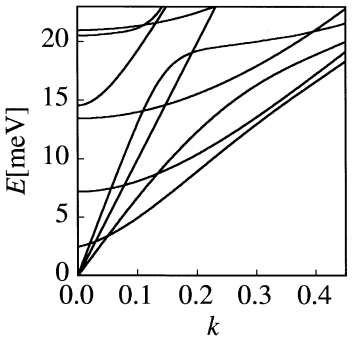

Fig. 8.5. The phonon-dispersion relations for a $(10, 10)$ carbon nanotube in a low-energy region near the Γ point [6], [11]. Shown are four acoustic phonon modes (two degenerate TA modes, one twist mode, and one LA mode, listed in order of increasing energy, respectively) and several lowest optical subbands including the radial breathing mode at $\omega(k = 0) \approx 20.5\,\mathrm{meV}$. [Courtesy of Millie Dresselhaus]

is related to a rigid rotation of the tube around the tube axis. This mode, corresponding to the in-plane transverse acoustic mode for 2D graphite, is called the twisting mode. The sound velocities of the transverse, twisting, and longitudinal acoustic modes for a $(10, 10)$ carbon nanotube are estimated to be $v_{\mathrm{TA}} = 9.43 \times 10^3\,\mathrm{m/s}$, $v_{\mathrm{TW}} = 15.0 \times 10^3\,\mathrm{m/s}$, and $v_{\mathrm{LA}} = 20.35 \times 10^3\,\mathrm{m/s}$, respectively.

Several lowest optical subbands obtained by the zone-folding of 2D graphite, are also shown in Fig. 8.5. Among them are included an E_{2g} mode at $\omega(k = 0) = \sim 17\ \mathrm{cm}^{-1} = 2.1\,\mathrm{meV}$, an E_{1g} mode at $\sim 118\,\mathrm{cm}^{-1} = 14.6\,\mathrm{meV}$, and an A_{1g} mode at $\sim 165\,\mathrm{cm}^{-1} = 20.5\,\mathrm{meV}$, which is the radial breathing mode corresponding to the *acoustic* mode showing a k^2 dependence in a graphene sheet. Some phonon bands, which have the same symmetry, show anticrossing behavior because they couple to each other, whereas the modes with different symmetries simply cross because they do not interact with each other.

8.2.2 Computational Methods

Here we describe several computational methods that calculate the thermal conductivity and its temperature dependence. The thermal conductivity tensor $\mathbf{\Lambda}$ is related to the thermal current density $\mathbf{J}$ and the temperature gradient ∇T by

$$\mathbf{J} = -\mathbf{\Lambda} \nabla T, \tag{8.21}$$

known as Fourier's definition of the thermal conductivity. If we consider the thermal conduction of a solid along a particular direction, for example, along the z-axis, the thermal conductivity κ can be expressed by combining

Eq. (8.21) with the continuity equation for heat conduction as

$$\frac{1}{A}\frac{dQ}{dt} = -\kappa\frac{dT}{dz}, \tag{8.22}$$

where dT/dz is the z-component of the temperature gradient and dQ is the heat flowing along the z-axis through the cross-sectional area A during the time interval dt.

Electrons and phonons, in principle, contribute to thermal conduction in solids. Both theoretical [14] and experimental studies [15], [16] show that the dominant contribution to heat conductance in graphite and nanotubes comes from phonons, whereas the contribution from electrons is extremely small even at low temperatures. In the following, we consider only the phonon contribution to thermal conduction in nanotubes.

The thermal conductivity κ is proportional to $\sum Cvl$, where C is the specific heat capacity, v the speed of sound, l the phonon mean free path, and $\sum$ means the summation over all phonon modes described in Sect. 8.2.1. The mean free path l can, in general, be determined from two contributions to the inelastic phonon scattering processes, which can be expressed as

$$\frac{1}{l} = \frac{1}{l_{\mathrm{st}}} + \frac{1}{l_{U\mathrm{m}}}. \tag{8.23}$$

where the first term l_{st} on the right-hand side is limited by scattering from sample boundaries (related to grain sizes) and defects, which are dominant at low temperatures. l_{st} is, therefore, independent of temperature so that the thermal conductivity κ shows its temperature dependence similar to that of the specific heat, C at low temperatures. On the other hand, the l_{Um} is determined by phonon-phonon Umklapp scattering that is dominant at high temperatures. As the temperature increases, the Umklapp scattering becomes more frequent, and thus it reduces l_{Um} further. At high temperatures, therefore, the temperature dependence of κ is expected to be dominated by l_{Um}. Such strong dependence of the thermal conductivity κ on l is demonstrated by the reported thermal conductivity values in the basal plane of graphite, which scatter by nearly two orders of magnitude [17]. Most factors determining the mean free path l of a sample, such as its grain size, sample quality, and isotope ratio, vary sample by sample.

We describe a few methods based on molecular dynamics simulations that have been used to calculate thermal conductivity of nanotubes.

8.2.2.1 Direct Molecular Dynamics Approach Based on Velocity Rescaling. To determine the thermal conductivity of nanotubes, we first used a method based on a direct molecular dynamics simulation, which had been successfully applied for glasses [18]. As illustrated schematically in Fig. 8.6(a), we consider a periodic array of hot and cold plates (e.g., a single circumferential ring in a nanotube) perpendicular to a direction (e.g., tube axis, z) along

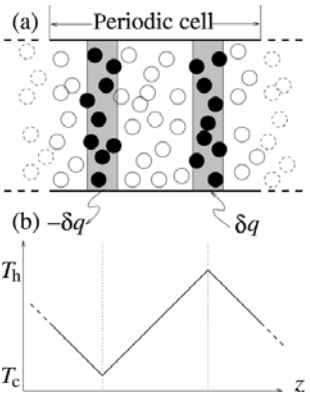

Fig. 8.6. (a) Schematic diagram of the direct molecular dynamics approach used to determine the thermal conductivity κ. Two gray regions represent the hot and cold plates maintained by subtracting δq from the energy of the particles in the cold one and adding it to that in the hot one. The particles in these two regions are depicted by a black solid circle. Through other particles depicted by an empty circle, heat gets transferred from the hot plate to the cold plate. (b) Ideal linear temperature profile along the z-axis, along which κ is being calculated.

which κ will be calculated. Heat exchange δq with hot and cold plates is achieved by velocity rescaling of particles in the plates. Due to the velocity rescaling, heat transfer is imposed, that is, thermal current flows between two regions. Once the system reaches a steady current state, one can determine thermal current density J_z along the z-direction to be $\delta q/(2A\Delta t)$, where A is a cross-sectional area of the hot plate and Δt is a time step for the molecular dynamic simulation. The thermal conductivity, then, can be calculated using Eq. (8.21), or

$$\kappa = -\frac{J_z}{\partial T/\partial z}, \tag{8.24}$$

when the z-component of the temperature gradient, $\partial T/\partial z$, does not vary significantly, as shown in Fig. 8.6(b), which exhibits an *ideal* linear temperature profile or a constant temperature gradient.

A real molecular dynamics simulation applied to a (10, 10) carbon nanotube, however, reveals a significant deviation from a stable linear temperature profile, as displayed in Fig. 8.7. In addition, the perturbations imposed by the heat transfer limit the effective phonon mean free path artificially below the unit cell size. Because the unit cell sizes tractable in our molecular dynamics simulations are significantly smaller than the phonon mean free path l of nanotubes, it has been found to be difficult to achieve the convergence of the simulations. Due to their high degree of long-range order, nanotubes exhibit an unusually long phonon mean free path l over hundreds of nanometers.

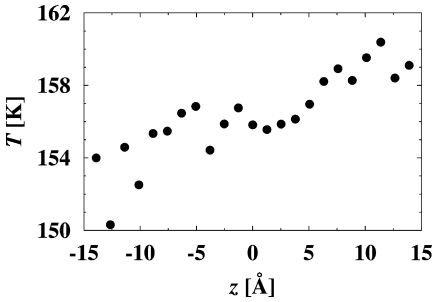

Fig. 8.7. Temperature profile of a (10, 10) nanotube along the tube axis.

8.2.2.2 Equilibrium Molecular Dynamics Simulations Based on the Green-Kubo Formalism. As an alternative approach determining the thermal conductivity, we used equilibrium molecular dynamics simulations [19], [20] based on the Green-Kubo relation for the Navier-Stokes thermal conductivity coefficient, which is derived in a relatively straightforward way from the Langevin equation [21]. The Green-Kubo expression relates the thermal conductivity to the integral over time t of the heat flux autocorrelation function by [21], [22]:

$$\kappa = \frac{1}{3Vk_BT^2}\int_0^\infty C(t)dt, \tag{8.25}$$

where k_B is the Boltzmann constant, V is the volume, T is the temperature of the sample, and $C(t)$ is the the heat-flux autocorrelation function given by

$$C(t) = \langle \mathbf{J}(t)\cdot\mathbf{J}(0)\rangle, \tag{8.26}$$

where the angled brackets $\langle\cdots\rangle$ denote an ensemble average. (It is usually very difficult to evaluate $C(t)$ quantum mechanically. Considering the quantum effects and the anharmonicity in the interaction potential, it has been proved that the classical autocorrelation function can be used with validity to calculate the thermal conductivity [23].) The heat-flux vector $\mathbf{J}(t)$ is defined by

$$\begin{aligned}\mathbf{J}(t) &= \frac{d}{dt}\sum_i \mathbf{r}_i\Delta e_i \\ &= \sum_i \mathbf{v}_i\Delta e_i + \sum_i\sum_{j(\neq i)} \mathbf{r}_{ij}(\mathbf{f}_{ij}\cdot\mathbf{v}_i),\end{aligned} \tag{8.27}$$

where $\mathbf{v}_i$ is the velocity of atom i and $\Delta e_i = e_i - \langle e\rangle$, the excess energy of atom i with respect to the average energy per atom $\langle e\rangle$. $\mathbf{r}_i$ is its position and $\mathbf{r}_{ij} = \mathbf{r}_i - \mathbf{r}_j$. Assuming that the total potential energy $U = \sum_i u_i$ can be expressed as a sum of binding energies u_i of individual atoms, $\mathbf{f}_{ij} = -\nabla_i u_j$, where ∇_i is the gradient with respect to the position of atom i.

Once $\mathbf{J}(t)$ is known, the thermal conductivity can be calculated using Eqs. (8.25) and (8.26). We found, however, that these results depend sensitively on the initial conditions of each simulation, thus necessitating a large ensemble of simulations. This high computational demand was further increased by the slow convergence of the autocorrelation function, requiring long integration time periods. This is illustrated in Fig. 8.8, which shows the autocorrelation function of a (10, 10) carbon nanotube as a function of time. The convergence has not been achieved even after several tens of thousands of molecular dynamics time steps of $\Delta t = 5 \times 10^{-16}$ sec. Moreover, because the autocorrelation function represents the average response to the fluctuation of the *equilibrium* system, which is fairly small, the signal-to-noise ratio is often small.

8.2.2.3 Nonequilibrium Molecular Dynamics Simulations Based on the Green-Kubo Formalism. To overcome these disadvantages, we now introduce an alternative approach [24] that uses molecular dynamics simulations based on *nonequilibrium* thermodynamics [25], [26]. It has been shown that this approach, developed in a computationally efficient manner [27], reduces the inefficiencies that occur in equilibrium approach. In the following, we describe briefly the nonequilibrium molecular dynamics simulations combined with the Green-Kubo formalism.

In this approach, the temperature T of the sample is regulated by a Nosé-Hoover thermostat [28], [29], which indicates the temperature of a surrounding thermal reservoir. An important fact that makes this approach *nonequilibrium* is the introduction of a small fictitious "thermal force," which improves the signal-to-noise level of the response dramatically. The fictitious thermal force $\mathbf{F}_e$, which has a dimension of *inverse length*, is equally applied to individual atoms. This fictitious force $\mathbf{F}_e$ and the Nosé-Hoover thermostat impose an additional force $\Delta\mathbf{F}_i$ on each atom i. This additional force modifies

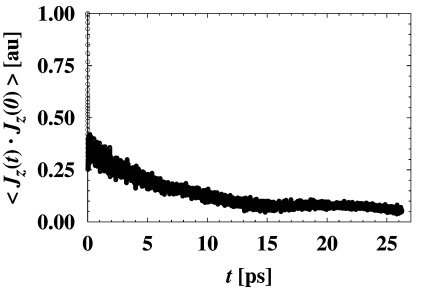

Fig. 8.8. Autocorrelation function calculated from the z-component of the heat flux vector, $J_z(t)$ for a $(10, 10)$ carbon nanotube.

the gradient of the potential energy and is given by

$$\Delta\mathbf{F}_i = \Delta e_i \mathbf{F}_e - \sum_{j(\neq i)} \mathbf{f}_{ij}(\mathbf{r}_{ij} \cdot \mathbf{F}_e) + \frac{1}{N} \sum_j \sum_{k(\neq j)} \mathbf{f}_{jk}(\mathbf{r}_{jk} \cdot \mathbf{F}_e) - \alpha \mathbf{p}_i. \tag{8.28}$$

Here, α is the Nosé-Hoover thermostat multiplier acting on the momentum $\mathbf{p}_i$ of atom i. α is calculated using the time integral of the difference between the instantaneous kinetic temperature T of the system and the heat bath temperature T_{eq}, from $\dot{\alpha} = (T - T_{eq})/Q$, where Q is the thermal inertia. The third term in Eq. (8.28) guarantees that the net force acting on the entire N-atom system vanishes. With the additional force $\Delta\mathbf{F}_i$ for a given value of $\mathbf{F}_e$, the heat-flux vector $\mathbf{J}(\mathbf{F}_e, t)$ is determined, for a given time t, using Eq. (8.28). The resulting thermal conductivity along the z-axis is given by

$$\kappa = \lim_{\mathbf{F}_e \to 0} \lim_{t \to \infty} \frac{\langle J_z(\mathbf{F}_e, t) \rangle}{F_e T V}, \tag{8.29}$$

where $J_z(\mathbf{F}_e, t)$ is the z-component of the heat-flux vector for a particular time t and V is the volume of the sample.

In low-dimensional systems, such as nanotubes or graphene monolayers, we infer the volume from the way these systems pack in space to convert thermal conductance of a system to thermal conductivity of a material. (Nanotubes form bundles and graphite forms a layered structure, both with an inter-wall separation of ≈3.4 Å.)

8.2.3 Thermal Conductivity of Carbon Nanotubes

We now present the results of nonequilibrium molecular dynamics simulations combined with the Green-Kubo formalism described in Sect. 8.2.2. We have used the Tersoff potential [30], [31], which has been augmented by van der Waals interactions fitted from interlayer interactions in graphite [32], for atomic interactions in the molecular dynamics simulations. The temperature dependence of the thermal conductivity of nanotubes and other carbon allotropes is presented. We show that isolated nanotubes are at least as good heat conductors as high-purity diamond. Our comparison with graphitic carbon shows that interlayer coupling reduces thermal conductivity of graphite within the basal plane by one order of magnitude with respect to the nanotube value, which lies close to that for a hypothetical isolated graphite monolayer.

In Figs. 8.9–8.11 we present the results of our nonequilibrium molecular dynamics simulations for the thermal conductance of an isolated $(10, 10)$ nanotube aligned along the z-axis. In our calculation, we consider 400 atoms per unit cell and use periodic boundary conditions. Our results for the time dependence of the heat current for the particular value $F_e = 0.2\,\text{Å}^{-1}$, shown

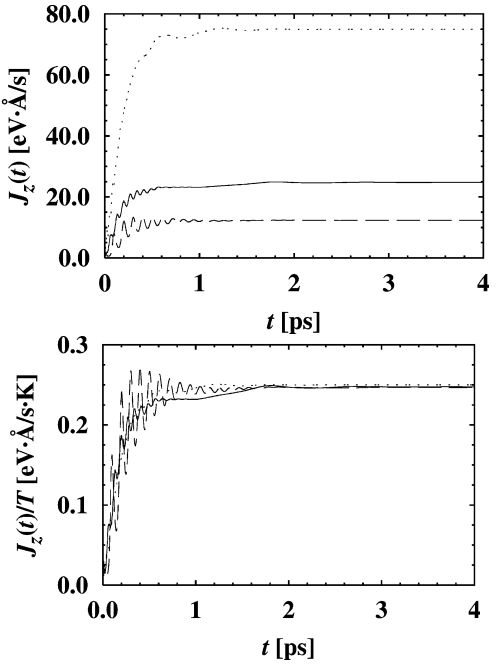

Fig. 8.9. (a) Time dependence of the axial heat flux $J_z(t)$ in a $(10, 10)$ carbon nanotube. Results of nonequilibrium molecular dynamics simulation at a fixed applied thermal force $F_e = 0.2\,\text{Å}^{-1}$, are shown at temperatures $T = 50\,\text{K}$ (dashed line), 100 K (solid line), and 300 K (dotted line). (b) Time dependence of $J_z(t)/T$, a key quantity for the calculation of the thermal conductivity, for $F_e = 0.2\,\text{Å}^{-1}$ and the same temperature values. (Reproduced from [33])

in Fig. 8.9(a), suggest that $J_z(t)$ converges within the first few picoseconds to its limiting value for $t \to \infty$ in the temperature range below 400 K. The same is true for the quantity $J_z(t)/T$, shown in Fig. 8.9(b), the average of which is proportional to the thermal conductivity κ according to Eq. (8.29). Each molecular dynamics simulation run consists of 50,000 time steps of $\Delta t = 5.0 \times 10^{-16}\,\text{s}$, or a total time length of 25 ps to represent the long-time behavior.

To study the F_e dependence of the thermal conductivity, we define a quantity by

$$\tilde{\kappa} \equiv \lim_{t\to\infty} \frac{\langle J_z(\mathbf{F}_e, t)\rangle}{F_e T V}. \tag{8.30}$$

In Fig. 8.10 we show the dependence of $\tilde{\kappa}$ on the fictitious thermal force. We have found that direct calculations of $\tilde{\kappa}$ for very small thermal forces carry a substantial error, as they require a division of two very small numbers in Eq. (8.30). Our calculations of the thermal conductivity at each temperature are based on 16 simulation runs, with F_e values ranging from 0.4–0.05 Å^{-1}.

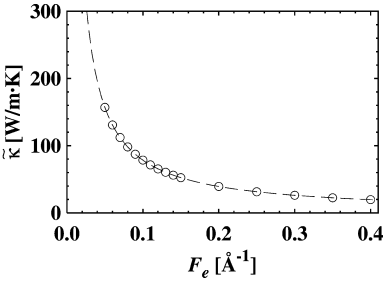

Fig. 8.10. Dependence of the heat transport on the applied heat force F_e in the simulations for $T = 100$ K. The dashed line represents an analytical expression that is used to determine the thermal conductivity κ by extrapolating the simulation data points $\tilde{\kappa}$ for $F_e \to 0$. (Reproduced from [33])

As shown in Fig. 8.10, data for $\tilde{\kappa}$ can be extrapolated analytically for $\mathbf{F}_e \to 0$ to yield the thermal conductivity κ, shown in Fig. 8.11.

Figure 8.11 also shows the temperature dependence of the thermal conductivity of an isolated (10, 10) carbon nanotube. The temperature dependence reveals the fact that κ is proportional to the heat capacity C and the phonon mean free path l. As we discussed, l is nearly constant at low temperatures, and the temperature dependence of κ follows that of the specific heat. At high temperatures, where the specific heat is constant, κ decreases as the phonon mean free path becomes smaller due to Umklapp phonon-phonon scattering processes. Our calculations suggest that at $T = 100\,\mathrm{K}$, carbon nanotubes show an unusually high thermal-conductivity value of $37{,}000\,\mathrm{W/m \cdot K}$. This value lies very close to the highest value observed in any solid, $\kappa = 41,000\,\mathrm{W/m \cdot K}$, which has been reported [5] for a 99.9% pure ^{12}C crystal at 104 K. In spite of the decrease of κ above 100 K, the room-temperature value of $6{,}600\,\mathrm{W/m \cdot K}$ is still very high, exceeding the reported thermal-conductivity value of $3{,}320\,\mathrm{W/m \cdot K}$ for nearly isotopically pure diamond [34]. Another theoretical study has shown that the thermal

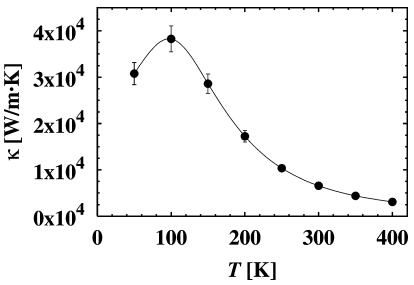

Fig. 8.11. Temperature dependence of the thermal conductivity κ for a (10, 10) carbon nanotube for temperatures below 400 K. (Reproduced from [33])

conductivity of a (10, 10) carbon nanotube approaches $\sim 2,980\,\mathrm{W/m \cdot K}$ along the tube axis [23].

Our theoretical prediction has been confirmed by an experimental measurement of the thermal conductivity of a *single* MWNT at mesoscopic scale [16]. The measured value has been reported to be $\kappa \gtrsim 3,000\,\mathrm{W/m \cdot K}$ near room temperature. We describe some details on this measurement in the next section.

It is useful to compare the thermal conductivity of a (10, 10) nanotube to that of an isolated graphene monolayer and bulk graphite. For the graphene monolayer, we unrolled the 400-atom large unit cell of the (10, 10) nanotube into a plane. The periodically repeated unit cell used in the bulk graphite calculation contained 720 atoms, arranged in three layers. The results of our calculations, presented in Fig. 8.12, suggest that an isolated nanotube shows very similar thermal-transport behavior to a hypothetical isolated graphene monolayer. Whereas even larger thermal conductivity should be expected for a monolayer than for a nanotube, we must consider that unlike the nanotube, a graphene monolayer is not self-supporting in a vacuum. For all carbon allotropes considered here, we also find that the thermal conductivity decreases with increasing temperature in the range depicted in Fig. 8.12.

Very interesting is the fact that once graphene layers are stacked in graphite, the interlayer interactions quench the thermal conductivity of this system by nearly one order of magnitude. For the latter case of crystalline graphite, our calculated thermal-conductivity values are in general agreement with available experimental data [35], [36], [37] measured in the basal plane of highest-purity synthetic graphite, which are also reproduced in the figure. We would like to note that experimental data suggest that the thermal conductivity in the basal plane of graphite peaks near 100 K, similar to our nanotube results.

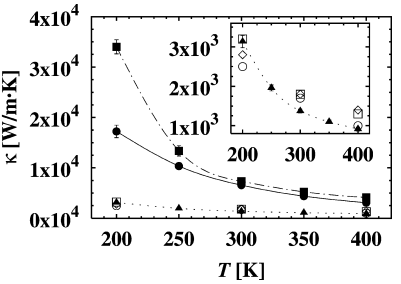

Fig. 8.12. Thermal conductivity κ for a (10, 10) carbon nanotube (solid line) in comparison to a constrained graphite monolayer (dash-dotted line) and the basal plane of AA graphite (dotted line) at temperatures between 200 K and 400 K. The inset reproduces the graphite data on an expanded scale. The calculated values are compared to the experimental data of [35] (open circles), [36] (open diamonds), and [37] (open squares) for graphite. (Reproduced from [33])

Based on the described difference in the conductivity between a graphene monolayer and graphite, we should expect a similar reduction of the thermal conductivity when a nanotube is brought into contact with other systems. This should occur when nanotubes form a bundle or rope or interact with other nanotubes in the "nanotube mat" of "bucky-paper" and could be verified experimentally. Consistent with our conjecture is the low value of $\kappa \approx 0.7\,\mathrm{W/m \cdot K}$ reported for the bulk nanotube mat at room temperature [15], [38].

In summary, we combined results of equilibrium and nonequilibrium molecular dynamics simulations with accurate carbon potentials to determine the thermal conductivity κ of carbon nanotubes and its dependence on temperature. Our results suggest an unusually high value $\kappa \approx 6,600\,\mathrm{W/m \cdot K}$ for an isolated (10,10) nanotube at room temperature, comparable to the thermal conductivity of a hypothetical isolated graphite monolayer or graphene. We believe that these high values of κ are associated with the large phonon mean free paths in these systems. Our numerical data indicate that in the presence of interlayer coupling in graphite and related systems, the thermal conductivity is reduced significantly to fall into the experimentally observed value range.

8.3 Experiments of Thermal Conduction in Carbon Nanotubes

In the previous section, we discussed theoretical prediction of unusually high thermal conductivity in nanotubes. In this section we discuss the experimental results of thermal conductivity in these materials. Experimentally, carbon-based materials, such as diamond and graphite (in-plane), have exhibited the highest measured thermal conductivity among the known materials at moderate temperatures [39]. The measured value of thermal conductivity of high-quality, 99.9% isotope-free diamond has been recorded up to 40,000 W/mK at 77 K and ∼3,000 at room temperature [5]. The in-plane thermal conductivity of graphite is very high: the values of room-temperature thermal conductivity obtained from single crystals and highly oriented pryolytic graphite (HOPG) were reported above 2000 W/m K [40]. Similar to graphite single crystals, a careful study on the axial thermal conductivity of vapor-grown graphite fibers with high-temperature heat treatments (∼3000°C) shows that the high thermal conductivity is closely related to the degree of graphitization, that is, the reduction of the grain-boundary density in the samples [41].

The thermal conduction is largely dominated by the phonon contribution in graphite. The electrical conduction is much poorer than that of most metals due to the semimetallic nature of the electron band structure of graphite with greatly reduced carrier density near the Fermi level. On the other hand, the stiff carbon-carbon bonds in graphitized planes increase the speed of sound, and thus, the phonon conduction in the graphite is greatly enhanced.

The thermal conductivity contributed by electrons, κ_{el}, can be estimated experimentally using the Wiedemann-Franz law:

$$\frac{\kappa_{el}}{\sigma T} = L_0, \tag{8.31}$$

where σ is the electrical conductivity and L_0 is the Lorenz number, $L_0 = 2.45 \times 10^{-8}\,(\mathrm{V/K})^2$. In graphite single crystals, it has been found from the thermal- and electrical-conductivity measurements that the phonon contribution of the thermal conductivity, κ_{ph}, dominates κ_{el} and thus $\kappa \approx \kappa_{ph}$ for $T > 20\,\mathrm{K}$ [40].

The discovery of carbon nanotubes [3] has led speculation that this new class of 1D materials could have a thermal conductivity greater than that of graphite due to the long-range crystalline order without boundaries and suppression of phonon-phonon scattering in one dimension [42]. The initially experimental efforts to measure the thermal conductivity of nanotubes have focused on the "bulk" measurements using milimeter-sized mats of nanotubes. The experiments on MWNTs [43] and SWNTs [15] showed the low-dimensional nature of the phonon conduction in these materials. However, the absolute value of the measured thermal conductivity of these bulk samples were two orders of magnitude smaller than theoretically expected values. Later, the improvement in sample preparation was made by aligning nanotubes using a high magnetic field. The measurements of these aligned nanotube samples showed a greatly enhanced measured thermal conductivity in these macroscopic samples allowing the heat flows preferentially along the tubes. Very recently, the group that one of the authors worked with demonstrated mesoscopic thermal conductivity measurements that probed the thermal conductivity of a single isolated MWNT. These results showed that the experimentally measured thermal conductivity of nanotubes is approaching the theoretical predictions as discussed in the previous section [16]. In this section, we discuss briefly the previous bulk thermal-conductivity measurements and then the details of the method and results of the mesoscopic thermal-transport measurements.

8.3.1 Bulk Thermal-Conductivity Measurements of Carbon Nanotubes

In bulk thermal-conductivity measurements of nanotubes, milimeter-sized mat samples are used in a conventional DC measurement setup with differential thermocouples of Ac 3ω method using self-heating of samples. Usually these bulk samples consist of networks of tightly packed nanotube bundles. The filling factor of the sample volume is one of the important factors in the estimation of thermal conductivity from a measured thermal conductance of the samples. Due to the large uncertainty in this filling factor estimation, it is often difficult to obtain the absolute values of the thermal conductivity of the bulk sample accurately. However, the temperature dependence is expected to be less affected by the uncertainty in the filling factor estimation.

The first thermal-conductivity measurements on bulk MWNTs samples were reported by Yi et al. [43] using the MWNTs synthesized by a chemical vapor deposition (CVD) method [44]. The sample consists of the MWNT's diameter ranges 20–40 nm, which correspond to 10–30 graphene walls along the tube axis. A self-heating 3ω method was used in this experiment to measure the thermal diffusivity and specific heat simultaneously. The thermal conductivity was estimated from these quantities considering the filling factor and the density of the sample. Figure 8.13 shows the resulting thermal conductivity of MWNT samples from 4 to 300 K. In the entire temperature range, the measured thermal conductivity, $\kappa(T)$, increases monotonically without any signature of saturation. The room-temperature thermal conductivity is $\sim$25 W/mK, which is much smaller than the theoretically predicted values.

It is interesting to compare $\kappa(T)$ obtained from this bulk MWNT measurement with $\kappa(T)$ observed in graphite fibers. In highly graphitic fibers, $\kappa(T)$ follows a $T^{2.3}$ temperature dependence until $T < 100$ K then begins to decrease with increasing T above $\sim$150 K [41]. The decrease in $\kappa(T)$ above 150 K is due to the onset of phonon-phonon Umklapp scattering. The Umklapp process becomes more effective with increasing temperature as higher-energy phonons are thermally populated. In less graphitic, and thus more disordered, fibers, however, the magnitude of κ is significantly lower and the Umklapp peak in $\kappa(T)$ is absent [41]. This drastic change of $\kappa(T)$ in disordered graphite fiber indicates that the Umklapp phonon scattering is much less important than the grain-boundary phonon scattering in the disordered samples. In the MWNT experiments discussed here, the behavior of $\kappa(T)$ resembles that of disordered graphitic fibers. The room-temperature thermal conductivity is smaller than that of the disordered graphitic fibers, and $\kappa(T)$ does not exhibit a peak due to Umklapp scattering; both properties are consistent with phonon scattering dominantly by the disorders in the samples.

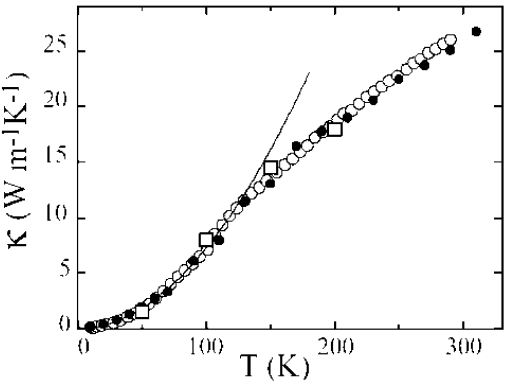

Fig. 8.13. Measured thermal conductivity of MWNTs mat samples at deferent temperatures. Solid line is fit by a T^2 curve up to 120 K. (Reproduced from [43])

Unlike these similarities in the high-temperature regime, the low-temperature behavior of $\kappa(T)$ observed in these bulk measurements is different from that of graphite fibers. At low temperatures ($T < 100$ K), $\kappa(T)$ of the MWNTs increases as $\sim T^2$ (solid line in Fig. 8.13) as opposed to $\sim T^{2.3}$ in graphite. One possible explanation for this difference in low-temperature behavior of $\kappa(T)$ is that the 2D nature of phonon conduction plays an important role in MWNTs. Because the thermal contacts between the MWNTs are only made through the outermost walls (thermal conduction is relatively poor across shells), only the outermost walls of MWNTs can contribute to the thermal-conductivity measurements. Because of the large diameter of MWNTs, phonons in the outermost walls essentially behave like a 2D phonon system. If this interpretation is correct, the magnitude of axial thermal conductivity of MWNTs can be much larger than the measured $\kappa(T)$. We discuss this interesting dimensional cross over in MWNT phonon transport later in this section in connection with the recent mesoscopic measurements.

We now discuss the experimental thermal conductivity of SWNT bulk samples. Compared to the MWNT mat samples, much effort has been made in SWNTs to improve the bulk sample quality for thermal transport measurements. Hone et al. first reported the measured thermal conductivity in an unaligned mat sample that consists of ropes of SWNTs average diameter 1.4 nm [15]. Later, Hone et al. reported much improved results using aligned SWNTs samples [45]. In the latter experiment, the SWNT ropes in the sample were aligned by a suspension deposition in a high magnetic field, followed by annealing the samples at 1200°C to help the tight packing of SWNT ropes in the sample. The very high density samples (about half the crystallographic value) were obtained in this method. A comparative DC technique and an AC self-heating method were used in low-temperature (10–300 K) and high-temperature (300–400 K) ranges, respectively. Figure 8.14 compares of measured thermal conductivity of these aligned and unaligned samples. The thermal conductivity, $\kappa(T)$, was measured along the aligning axis for the aligned sample. Although the temperature dependence of $\kappa(T)$ is similar for both 1.4-nm-diameter SWNT samples, the magnitude of $\kappa(T)$ is very sensitive to the disorderness of samples. In unaligned disordered samples, the room-temperature thermal conductivity is only $\sim$35 W/m K, while the aligned and less disordered sample shows the thermal conductivity higher than 200 W/m K. This observation implies that the numerous junctions in nanotubes mat are the dominant thermal resistance source for the bulk thermal conductivity measurements. At room temperature, $\kappa(T)$ of the aligned SWNT sample is still an order of magnitude smaller than that of diamond or graphite (in-plane). Above 300 K, $\kappa(T)$ increases slowly and then levels off near 400 K. Graphite and diamond, on the other hand, show a decreasing $\kappa(T)$ with increasing temperature above $\sim$150 K due to phonon-phonon Umklapp scattering, as we discussed earlier.

This absence of the Umklapp scattering peaks in $\kappa(T)$ of SWNTs ropes implies that the dominant phonon-scattering source in a rope of SWNTs is

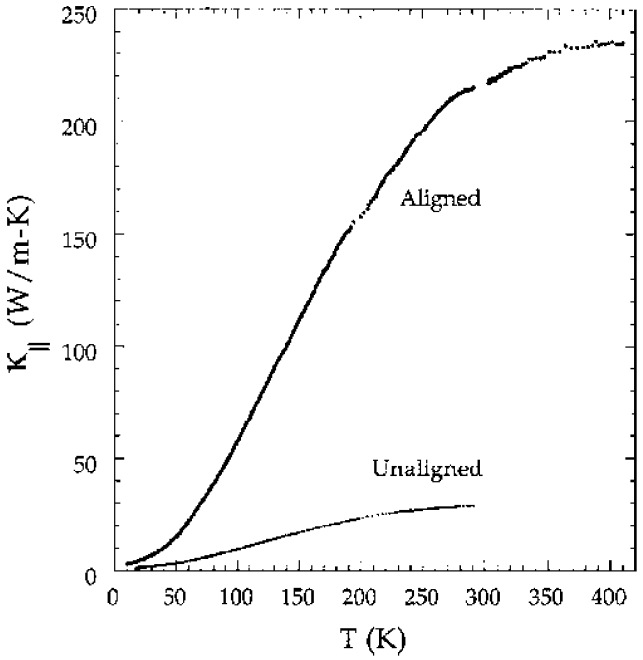

Fig. 8.14. Thermal conductivity of the aligned and unaligned SWNT bulk samples. The thermal conductivity was measured parallel to tube direction for the aligned sample. (Reproduced from [45])

defects or boundary-scattering-related mechanism rather than phonon-phonon interaction. Although an isolated SWNT does not have a boundary that a phonon can scatter off, a rope of SWNT has its boundary that a long wavelength phonon can scatter off. In addition, the restricted geometry of the SWNTs may also affect the Umklapp scattering process. In 1D systems, Umklapp scattering is expected to be suppressed due to the low availability of appropriate phonons for conservation of energy and wave vector [46]. This inherent suppression of phonon-phonon scattering in one dimension can be the alternative explanation of the observed absence of Umklapp scattering peak in $\kappa(T)$. More quantitative work should elucidate this important issue, extending this measurement to higher temperatures and using SWNT bulk samples with different diameters and disorderness.

The low-temperature behavior of $\kappa(T)$ of SWNT samples deserves more attention. As highlighted in Fig. 8.15, $\kappa(T)$ of SWNT bulk samples shows a linear temperature dependence below $\sim$35 K. This linear T dependence of $\kappa(T)$ at low temperature reflects the 1D phonon band structure of individual SWNTs [47]. At low temperatures, only the four acoustic phonon modes are thermally populated, while at slightly higher temperatures the lowest zone-folded phonon subband begins to be populated [11]. $\kappa(T)$ can be modeled

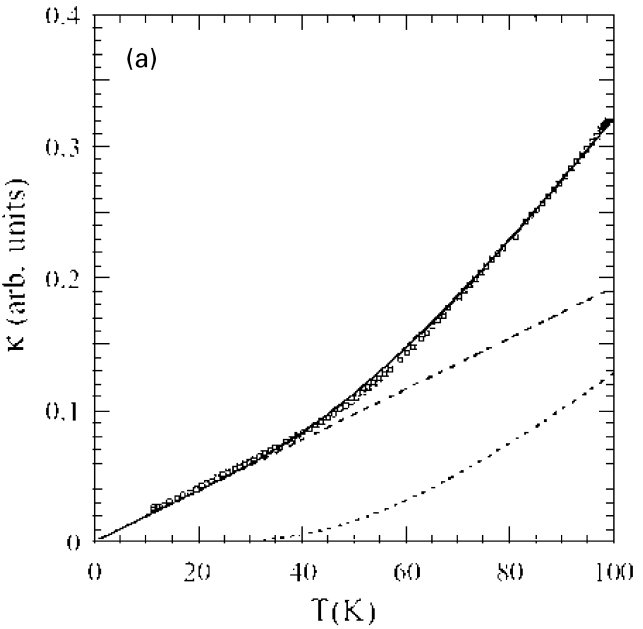

Fig. 8.15. Temperature-dependent thermal conductivity of SWNTs at low-temperature regime. The linear broken line represents the contribution from the acoustic band, and the quadratic dotted line corresponds to the contribution from the first subband in the two- band model (see text for details). The solid line is the sum of the two contributions compared to the measurements (circles). (Reproduced from [47])

using a simplified two-band model, considering only an averaged single acoustic band and one zone-folded subband. In a simple zone-folding picture, the acoustic band has a dispersion relation $\omega = vk$ and the first subband has dispersion relation $\omega^2 = v^2k^2 + \omega_0^2$, where $w_0 = v/R$, and R and v are the radius and sound velocity of the sample, respectively. The thermal conductivity from each band can then be estimated using these dispersion relations [47]. The solid line in Fig. 8.15 shows a fit with this two-band model with the parameters v and $\hbar\omega_0/k_B$ chosen to be 20 km/s and 35 K, respectively [47]. These choices are within a reasonable range considering that the sound speed of two acoustic modes in nanotubes are 15 km/s (twist mode) and 24 km/s (longitudinal mode) [11]. Note that in this model, the contribution from the lowest optical subband freezes out at temperatures below $\sim$35 K as indicated by the dotted line in the figure. Below this temperature, $\kappa(T)$ shows a linear T dependence. A similar linear T dependence of $\kappa(T)$ was observed in micromachined silicon nitride membrane at very low temperatures ($<$0.6 K) and has been interpreted as the signature of the quantization of phonon thermal conductance in a 1D system [48]. Although the absolute value of $\kappa(T)$ of an individual SWNT was not obtained in the bulk measurements, qualitatively, this linear T behavior

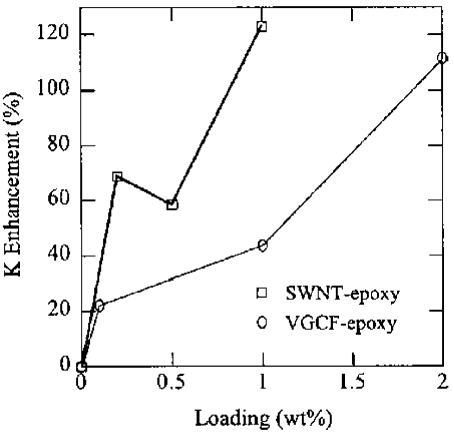

Fig. 8.16. Enhancement in thermal conductivity relative to pristine epoxy as a function of SWNT and vapor-grown carbon fiber (VGCF) loading. (Reproduced from [49])

of the SWNTs $\kappa(T)$ below 35 K strongly suggests that the phonon conduction may be quantized in SWNTs. Extremely restricted phonon-transport channels and absence of the boundary scattering make such quantization occur at relatively elevated temperatures in SWNTs. Thermal-conductance measurement on an isolated SWNT should address this interesting problem in the future.

In addition, SWNTs were used to augment the thermal-transport properties of industrial epoxy [49]. Figure 8.16 shows the thermal conductivity enhancement in this SWNT-epoxy composite material. Epoxy matrixes loaded with 1 wt% SWNTs show a 70% increase in thermal conductivity at 40 K, rising to 125% at room temperature (squares). As shown in the same graph for a comparison, the enhancement due to 1 wt% loading of vapor-grown carbon fibers is three times smaller (circles). These results suggest that the thermal-conduction properties of epoxy composites are significantly enhanced by optimally introduced highly thermal-conductive nanotubes into the epoxy matrix, and SWNTs are much more effective for this than larger-diameter carbon fibers.

8.3.2 Experimental Method for the Mesoscopic Thermal Transport Measurement

Although the previously mentioned bulk studies have provided a qualitative understanding of the thermal properties of these materials, there are significant disadvantages to these macroscopic measurements for understanding intrinsic thermal properties of a single nanotube. One problem is that these measurements yield an ensemble average over the different tubes in a sample. Moreover, in thermal-conductivity measurements, it is difficult to extract

absolute values for these quantities due to the presence of numerous tube-tube junctions. These junctions are in fact the dominant barriers for thermal transport in a mat of nanotubes. Most importantly, it is only at the mesoscopic scales where one can study the quantum limit of energy (thermal) transport. In this regard, the mesoscopic thermal-transport measurements are necessary to elucidate the intrinsic thermal properties of nanotubes. Thanks to the advances of modern semiconductor process technology, such mesoscopic experiments on semiconducting devices have been recently demonstrated [48]. Inspired by this work and using novel hybridized synthesis techniques in combination with semiconductor device fabrication techniques, one of the authors recently demonstrated mesoscopic thermal transport in carbon nanotubes [16]. In this subsection, we discuss this novel method, which allows us to probe the thermal-transport properties of nanotubes at mesoscopic scales.

For small-signal thermal-transport measurements, AC thermal transient techniques, such as the self-heated 3ω method [43], [50] are often used to enhance measurement precision. In these methods, an AC heating current with a frequency ω is applied to generate an oscillating thermal energy flow at a frequency 2ω in the sample. Because the propagation of the heat wave is related to the thermal diffusivity and the thermal conductivity of the sample, measuring this wave propagation as a function of ω will provide the values of these quantities [43]. The measurement of the heat wave propagation can be achieved by probing the amplitude and phase of the third-order harmonics (3ω) in the heater voltage. This 3ω voltage fluctuation is caused by the resistance change of the heater itself due to the 2ω fluctuation in temperature. It has been successfully demonstrated that this AC 3ω method can be used to measure the thermal conductivity of bulk nanotube samples [43], [45]. However, it is difficult to apply this 3ω method directly to a mesoscale measurement due to the limited dimension of samples. Especially, for individual nanotubes with a usual length of 1–10 μm, the required frequency to observe the changes in amplitude and phase of heat-wave propagation is more than 100 MHz. Such high frequency thermal-transport measurements are very difficult to realize in a mesoscopic scale. Therefore, a conventional steady-state measurement technique is suitable to probe the thermal conduction through a nanotube at mesoscopic scales.

Figure 8.17 shows a schematic for the steady-state thermal- transport measurements. A sample is clamped between the two thermal reservoirs at the temperatures T_h and T_c, respectively. Thermal energy is supplied from the heat reservoir on the left side so that $T_h \geq T_c$. To measure the heat flow, Q, through the sample, a calibration reference with a known thermal conductance, K_0, is connected between the cold reservoir (T_c) and the heat sink at temperature T_0 ($T_c > T_0$). The thermal conductance of the sample, K_s, is obtained by $K_s = K_0(T_h - T_c)/(T_c - T_0)$. This simple experimental scheme works only if: (1) all the heat flow through the sample flows through the calibration reference, (2) K_s is not too small compared to K_0. The latter condition ensures that the measurement has a high enough signal-to-noise ratio.

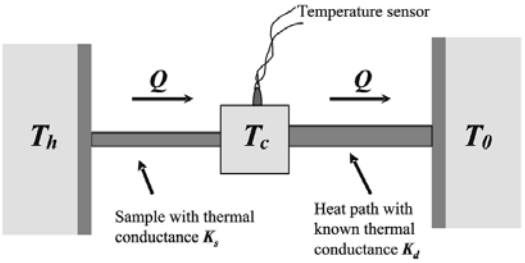

Fig. 8.17. Schematic for experimental setup of steady-state thermal-conductivity measurements.

These two conditions put the following stringent requirements for the thermal conduction measurements at mesoscopic scales. First, the device for measuring temperatures and applying heat should be suspended and free from substrate contact except through small but well-controlled thermal pathways. Therefore, the experiment should be carried out under high vacuum to suppress the residual gas conduction. The radiational heat loss at high temperature ranges should also be considered carefully. These requirements reduce the parasite heat loss from the thermal paths and allow the first condition to hold at mesoscopic scales. For example, the thermal conductance due to residual gas conduction of air, $K_{\rm gas}$, is estimated from a simple kinetic theory:

$$K_{\rm gas} \approx 10^{-5} \times \frac{P(\text{torr})\ l_c(\mu\text{m})}{\sqrt{T/300K}}\ \text{Watt/K}, \tag{8.32}$$

where P is pressure and l_c is the characteristic length scale of the measuring device. For isolated nanotubes, we expect $K_s \lesssim 10^{-7}$ Watt/K, while $l_c \sim 10\,\mu$m. Thus $P \ll 10^{-4}$ torr is required for room-temperature measurements. For the thermal-transport measurements in the ultimate quantum limit, $K_s \sim 10^{-12}$ Watt/K at 1 K [48], and hence $P \sim 10^{-9}$ torr is required. On the other hand, the radiational heat loss, $K_{\rm rad}$, from the surface of the mesoscopic sample is not significant compared to $K_{\rm gas}$. Due to the greatly reduced surface area in this mesoscopic measurement, $K_{\rm rad} \leq 10^{-13}$ Watt/K even at 300 K for an isolated nanotube sample.

In addition, very thin and long bridges are required to suspend the heaters, thermometers, and samples to achieve the condition $K_s \sim K_0$. For example, a patterned silicon nitride strip with cross-sectional area $1 \times 1\,\mu\text{m}^2$ and length 200 μm provides $K_0 \sim 10^{-7}$ Watt/K at room temperature, which is compatible for an isolated MWNT measurement ($K_s \sim 10^{-8}$ Watt/K), but still too large for a single SWNT measurement ($K_s \sim 10^{-10}$ Watt/K). Furthermore, the metal lines that connect the heater lines and the thermometer should be designed to meet the second condition, especially for low temperatures where electron thermal conduction becomes important compared to the phonon counterpart. For extremely low-level signal measurements, such as the quantized thermal-conductance experiment ($K_0 \sim 10^{-13}$ Watt/K),

superconducting leads that completely remove the electronic thermal conduction should be used [48].

Thanks to the advances MEMS technology, the aforementioned suspended devices for the mesoscopic thermal-transport measurement are possible. Recent work on the thermal-conductivity measurement in an isolated MWNT used this advantage [16]. In this experiment, suspended structures were fabricated on a silicon nitride/silicon oxide/silicon multilayer substrate. A low-stress silicon nitride 0.5-μm-thick layer and a 10-μm-thick silicon oxide layer were grown on a silicon wafer by the CVD method. The microscopic Pt/Cr heaters, thermometers, and lead lines were fabricated by electron beam lithography. After fabricating metallic structures, the silicon nitride layer was patterned by photolithography followed by a reactive ion etching that anisotropically etches away exposed silicon nitride layer. In the final step, the silicon oxide sacrificial layer is etched away by HF wet etching, followed by a critical point-drying process. The resulting microdevices were suspended 10 μm above the underlying silicon substrate.

Figure 8.18 shows a representative device, including two 10-μm × 10-μm adjacent silicon nitride membrane (0.5-μm-thick) islands suspended with 200-μm-long silicon nitride beams. On each island, a Pt/Cr thin film resistor,

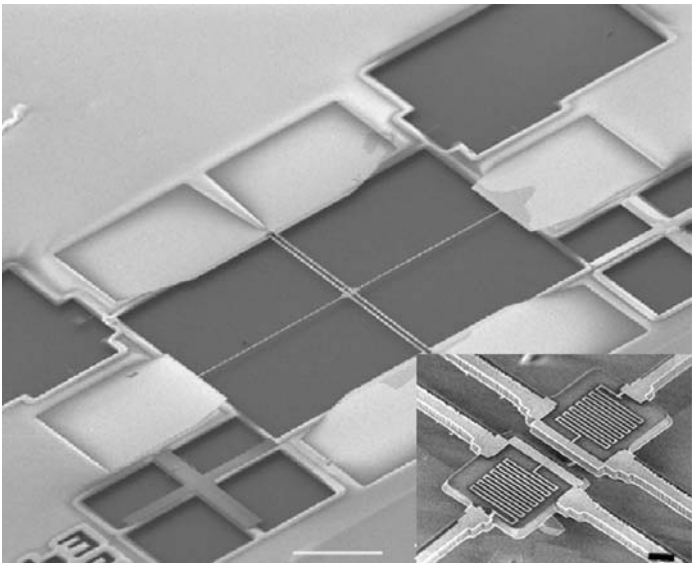

Fig. 8.18. A large-scale scanning electron microscopy (SEM) image of a microfabricated suspended device. Two independent islands are suspended by three sets of 250-μm-long silicon-nitride legs with Pt/Cr lines that connect the microthermometer on the islands to the bonding pads. The scale bar represents 100 μm. The inset shows an enlarged central part of the suspended islands with the micro resistors. The scale bar represents 1 μm. (Reproduced from [16])

fabricated by electron beam lithography, serves as a heater to increase the temperature of the suspended island. These resistors are electrically connected to contact pads by the metal lines on the suspending legs. Because the resistance of the Pt/Cr resistor changes with temperature, they also serve as a thermometer to measure the temperature of each island.

Once such suspended devices are fabricated, the mesoscopic thermal transport in nanotubes and nanowires can be probed as described later. The mesoscopic sized samples are placed on the device and form a thermal path between two suspended islands that are otherwise thermally isolated from each other. Figure 8.19 shows a simple schematic for the heat transfer in such a hybrid device. The islands with heater resistor, R_h, and temperature sensor resistor, R_s, are suspended by beams with the total thermal conductance K_d for each island. A bias voltage applied to one of the heater resistors, R_h, creates Joule heat and increases the temperature, T_h, of the heater island from the thermal bath temperature T_0. Under steady state, there is heat transfer to the other island through the sample with the thermal conductance of the connecting sample, K_s, and thus the temperature, T_s, of the resistor R_s also rises. One can use a linear heat-transfer model to extract K_s and K_d, from the relations of the temperature increases as a function applied to heating power, W:

$$T_h = T_0 + \frac{K_d + K_s}{K_d(K_d + 2K_s)}W; \quad T_s = T_0 + \frac{K_s}{K_d(K_d + 2K_s)}W. \tag{8.33}$$

It is worth noting that in the derivation of this equation we assumed that each suspended island is in thermal equilibrium at temperature T_h and T_s, respectively. This assumption is valid for $K_s < K_d$, which generally holds for most nanoscale material measurements we discuss.

These suspended structures have been used to measure the thermal conductivity and thermoelectric power of nanotubes [16] and nanowires [51]. Mechanical manipulation similar to that used for the fabrication of nanotube scanning probe microscopy tips [52] has been used to place nanotubes and nanowires on the desired part of the device. This approach routinely produces a MEMS-nanotube/nanowire hybrid device that can be used to measure the

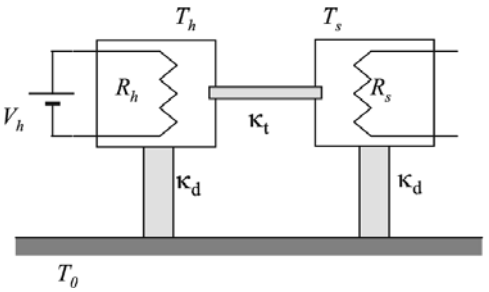

Fig. 8.19. Schematic heat-flow model of the suspended device with a sample across the two islands.

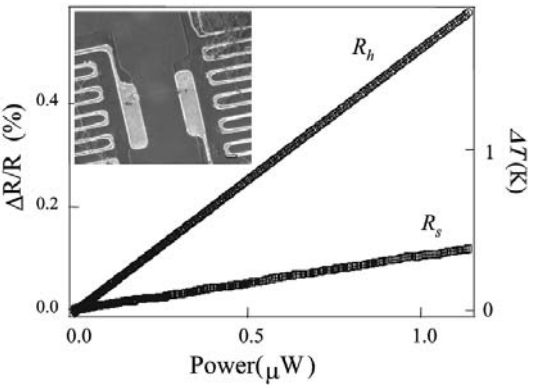

Fig. 8.20. The change of resistance of the heater resistor (R_h) and sensor resistor (R_s) as a function of the applied power to the heater resistor with a silicon nanowire bridging the two islands. The inset shows a detailed SEM image of the device. The scale bar represents 1 μm.

thermal conductivity and thermoelectric power of the bridging nanomaterials. Shown in the upper panel of Fig. 8.20 is an example of such a device with a silicon nanowire. The silicon nanowire with a diameter ∼50 nm is bridging the two suspended islands with microfabricated heaters (inset). The graph shows the temperature changes of each suspended island connected by this nanowire as a function W at room temperature. From the slopes of R_s and R_h versus W, K_s and K_d at temperature T_0 can be computed using Eq. 8.33. By measuring the samples diameters and length, the thermal conductivity of the sample can be estimated at different temperatures.

8.3.3 Thermal Conductivity of Multiwalled Nanotubes

In this subsection, we discuss the experimental results of mesoscopic thermal conductance measurement of MWNTs using the suspended devices described in the previous subsection. The thermal conductivities of small bundles of MWNTs and an isolated MWNT sample are presented.

Figure 8.21 displays the image of the MEMS-nanotube hybrid device that was used for the thermal conductance measurement of a single MWNT. The MWNT in this device has a 14-nm diameter and a 2.5-μm length of the bridging segment. The thermal conductance, K_s, was measured as described in the previous section in the temperature range 8–370 K. Below 8 K, both R_s and R_h become saturated due to the impurity scattering in Pt/Cr resistors and cannot be used for a temperature sensor. To ensure that the measurement remains in the linear response regime, W was limited to make $T_h - T_0 < 1$ K during the measurement. The measured K_s increases by several orders of magnitude as the temperature is raised, reaching a maximum of approximately

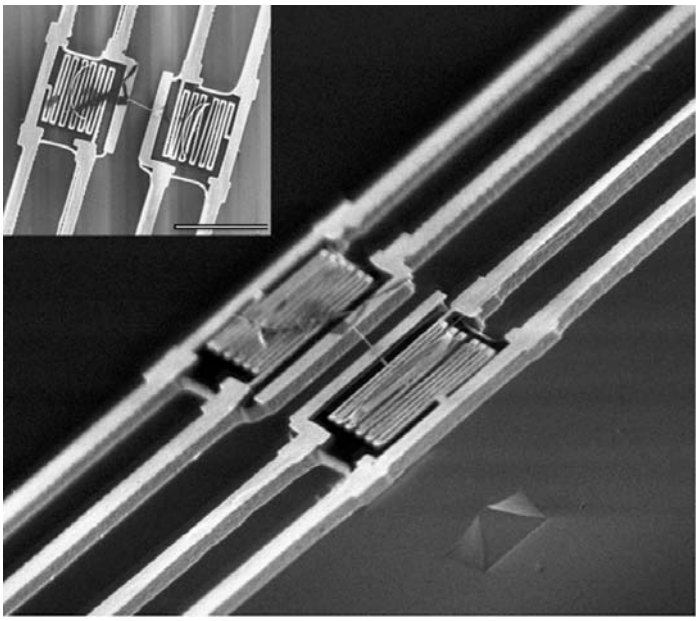

Fig. 8.21. SEM image of the suspended islands with a bridging individual MWNT. The diameter of the MWNT is 14 nm. The inset shows the top view of the device. The scale bar represents 10 μm.

1.6×10^{-7} W/K near room temperature before decreasing again at higher temperatures.

This measured thermal conductance includes the thermal conductance of the junction between the MWNT and the suspended islands in addition to the intrinsic thermal conductance of the MWNT itself. From a study of scanning thermal microscopy on a self-heated MWNT, the thermal conductance of the nanotube-electrode junction at room temperature was estimated; the heat-flow rate from a unit length of the tube to metal electrode at a given unit junction temperature difference was found to be ~ 0.5 W/m K. Considering the contact length of the MWNT to the electrodes on the islands is ~ 1 μm, the junction thermal conductance is $\sim 5 \times 10^{-7}$ W/K at room temperature. Because the total measured thermal conductance is 1.6×10^{-7} W/K, this suggests that the intrinsic thermal conductance of the tube is the major part of the measured thermal conductance.

To estimate thermal conductivity from the measured thermal conductance, we have to consider the geometric factors of the MWNT and the anisotropic nature of thermal conductivity. The outer walls of the MWNT that make good thermal contacts to a thermal bath contribute more in thermal transport than the inner walls, and the ratio of axial to radial thermal conductivity may influence the conversion of thermal conductance to thermal conductivity. Although the anisotropic electronic transport in MWNTs

has been studied recently [54], the anisotropic nature of thermal transport in MWNTs has not been studied to date. Without knowing this anisotropic ratio of MWNT thermal conductivity, it would be the first-order approximation to estimate the averaged thermal conductivity, assuming a solid isotropic material to consider geometric factors. This simplification implies that the thermal conductivity estimated in this work is a lower bound of the intrinsic axial thermal conductivity of an MWNT. Further study to analyze the contribution of individual layers of MWNTs in the thermal transport should elucidate this important issue in the future. Another major factor of uncertainty to determine the thermal conductivity arises from the uncertainty in diameter measurement. A high-resolution SEM was used to determine the diameter of the MWNT in this device. For MWNTs with ∼10 nm diameter, the resulting uncertainty in thermal conductivity can be as high as 50% of the estimated value.

Shown in Fig. 8.22 is the temperature-dependent thermal conductivity, $\kappa(T)$, of the isolated MWNT in Fig. 8.21. This result shows remarkable differences from the previous "bulk" measurements as described here. First, the room-temperature value of $\kappa(T)$ is greater than 3000 W/m K, whereas the

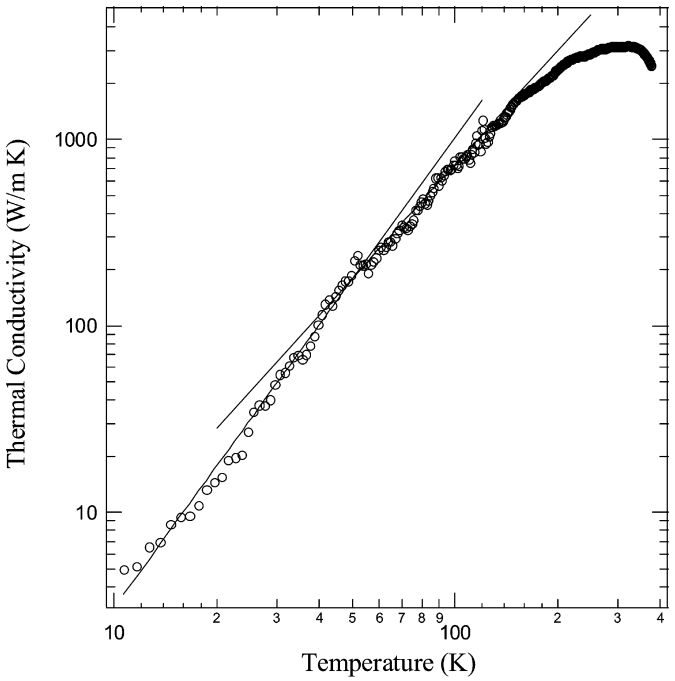

Fig. 8.22. The thermal conductance of an individual MWNT of 14-nm diameter. The solid lines represent linear fits of the data in a logarithmic scale at different temperature ranges. The slopes of the line fits are 2.50 and 2.01, respectively.

previous "bulk" measurement on an MWNT mat using the 3ω method estimated only $20\,\mathrm{W/m\,K}$ [42]. Note that our observed value is also an order of magnitude higher than that of aligned SWNT samples ($250\,\mathrm{W/m\,K}$) [44] but comparable to the theoretical expectation, $6000\,\mathrm{W/m\,K}$ as described in the previous section. This large difference between single-tube and "bulk" measurements suggests that numerous highly resistive thermal junctions between the tubes largely dominate the thermal transport in mat samples. Second, $\kappa(T)$ shows interesting temperature-dependent behavior that was absent in "bulk" measurement. As shown in this log-log plot, at low temperatures, $8\,\mathrm{K} < T < 50\,\mathrm{K}$, $\kappa(T)$ increases following a power law with exponent 2.50. In the intermediate temperature range ($50\,\mathrm{K} < T < 150\,\mathrm{K}$), $\kappa(T)$ increases almost quadratically in T (i.e., $\kappa(T) \sim T^2$). Above this temperature range, $\kappa(T)$ deviates from quadratic temperature dependence and has a peak at 320 K. Beyond this peak, $\kappa(T)$ decreases rapidly.

This observed behavior of the thermal conductivity can be understood by considering the dimensionality changes in the MWNT phonon system and Umklapp phonon scattering. In a simple model, the phonon thermal conductivity can be written as

$$\kappa = \sum_p C_p v_p l_p, \tag{8.34}$$

where C_p, v_p, and l_p are the specific heat capacity, phonon group velocity, and mean free path of phonon mode p, respectively. The phonon mean free path consists of two contributions—$l^{-1} = l_{st}^{-1} + l_{um}^{-1}$, where l_{st} and l_{um} are static and Umklapp scattering length, respectively. At low temperatures, the Umklapp scattering freezes out, $l = l_{st}$, and thus $\kappa(T)$ simply follows the temperature dependence of C_ps. For MWNTs, below the Debye temperature of interlayer phonon mode, $\Theta_\perp$, $\kappa(T)$ has a slight three-dimensional nature, and $\kappa(T) \sim T^{2.5}$ as observed in graphite single crystals [40]. As $T > \Theta_\perp$, the interlayer phonon modes are fully occupied, and $\kappa(T) \sim T^2$, indicative of the 2D nature of thermal conduction in an MWNT. From this cross-over behavior of $\kappa(T)$, we estimate $\Theta_\perp = 50\,\mathrm{K}$. This value is comparable to the value obtained by a measurement of specific heat of MWNT [43]. At very low temperatures, one should expect that the phonon transport is quantized as was observed in [48]. The thermal effects of 1D phonon quantization in a nanotube should be measurable as $T < T_{1D} = hv/k_B R$, where h is the Plank constant, k_B is the Boltzman constant, and R is diameter of the nanotube. For an MWNT with 10-nm diameter, however, T_{1D} is estimated to be $\sim 3\,\mathrm{K}$, which is the temperature range in which the experiments could not be carried out. Above this temperature, phonon transport in an MWNT essentially behaves like in a 2D graphene sheet as we discussed earlier.

As T increases, the strong phonon-phonon Umklapp scattering becomes more effective as higher energy phonons are thermally populated. Once $l_{st} > l_{um}$, $\kappa(T)$ decreases as T increase due to rapidly decreasing l_{um}. At the peak value of $\kappa(T)$, where $l_{st} \sim l_{um}$ ($T = 320\,\mathrm{K}$), we can estimate the

T-independent $l_{st} \sim 500\,\text{nm}$ for the MWNT using Eq. (8.34). Note that this value is an order of magnitude higher than previous estimations from "bulk" measurements [44] and is comparable to the length of the measured MWNT ($2.5\,\mu\text{m}$). Thus, below room temperature where the phonon-phonon Umklapp scattering is minimal, phonons have only a few scattering events between the thermal reservoirs, and the phonon transport is nearly ballistic. This remarkable behavior was not seen in the bulk experiments, possibly due to additional extrinsic phonon-scattering mechanisms such as tube-tube interactions.

It is also interesting to estimate the electrical contribution of thermal conductivity experimentally, κ_{el}, using the Wiedemann–Franz law. The measured electrical resistance of the MWNT is $\sim 35\,\text{k}\Omega$, and thus, $\kappa_{el}/\kappa \sim 10^{-3}$ at room temperature. This ratio is found to be even smaller at lower temperatures. Therefore, the thermal transport is completely dominant in all temperature ranges in nanotubes.

Finally, we discuss the diameter-dependent effects in $\kappa(T)$ of MWNT bundles. In most materials, decreasing size of the sample increases the surface-to-volume ratio and thus increases the phonon-scattering rate by the surface boundary. This effect is clearly shown in Fig. 8.23(a), which displays measured $\kappa(T)$ of silicon nanowires with different diameters [51]. As the diameter of silicon nanowire decreases, $\kappa(T)$ decreases drastically. This result clearly demonstrates the suppression of phonon transport due to the increased boundary scattering in small-diameter nanowires. The size dependent effect is completely opposite in the nanotube samples. Figure 8.23(b) displays the measured $\kappa(T)$ of MWNT bundles with different diameters. Surprisingly, $\kappa(T)$ increases as the diameter of the bundle decreases, as opposed to the silicon nanowire example. This interesting behavior arises from the peculiar geometry of nanotubes. Unlike nanowires, nanotubes have no boundary at the surface. A seamless graphitized wall of nanotubes provides phonon transport along the

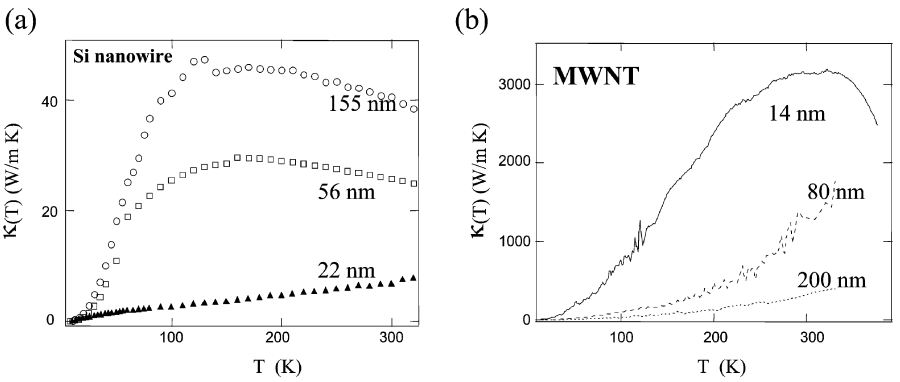

Fig. 8.23. (a) Thermal conductivity of silicon nanowires with different diameters. (Reproduced from [51]); (b) thermal conductivity of MWNT bundles with different diameters. (Reproduced from [16])

tube axis without phonon boundary scattering caused by "surface". Bundling individual nanotubes, on the other hand, creates a new phonon-scattering source by the intertube interaction and reduces the thermal conduction in the sample. Indeed, this experimental observation strongly suggests that the thermal conductivity of an SWNT might be even higher than that of an MWNT due to the absence of intershell phonon scattering as proposed by the theory in the previous section.

8.4 Summary and Future Work

We have presented both theoretical and experimental studies of thermal conduction in carbon nanotubes. The molecular dynamic simulations suggest a thermal conductivity of SWNTs up to 6600 W/mK at room temperature. This unusually high thermal conductivity of nanotubes is associated with the large phonon mean free paths in these systems. The mesoscopoic experimental study in MWNTs indeed confirms this theoretical expectation, showing that the measured values are of the same orders of magnitude. The observed thermal conductivity of an MWNT is more than 3000 W/m K at room temperature and the phonon mean free path is ∼500 nm. The temperature dependence of the thermal conductivity shows a peak at 320 K due to the onset of Umklapp phonon scattering. This observation strongly suggest that the phonon Umklapp process might be suppressed in this system due to the effectively reduced dimensionality. Although the theoretically predicted thermal conductivity of SWNTs is in good agreement with the experimentally measured value on MWNTs, we will perform more realistic theoretical calculations on MWNTs to understand some different features on the temperature dependence of thermal conductivity observed between calculations and measurements.

Of particular interest are mesoscopic thermal-transport measurements in SWNTs. The quantization of the phonon degrees of freedom has been shown to modify the heat capacity [45]. This quantization should lead to the thermal-conductance quantization, as shown in other 1D phonon-transport systems at low temperatures [48]. In addition, an extremely long phonon mean free path is expected in an isolated single SWNT due to the absence of intershell phonon scattering and further suppression of Umklapp process in this 1D nanoscale system. Experiments attempting to measure these unique phenomena in SWNTs are underway in one of the authors' group.

Acknowledgments

The authors wish to thank Savas Berber, David Tománek, L. Shi, A. Majumdar, P. L. McEuen and Seung-Hoon Jhi for helpful discussion.

The authors also acknowledge that the work described here has been done in collaboration with Berber, Tománek, Shi, Majumdar, and McEuen. Special thanks go to D. Li and A. Majumdar for sharing the data before publication.

References

[1] M. S. Dresselhaus, G. Dresselhaus, and P. C. Eklund, *Science of Fullerenes and Carbon Nanotubes*. Academic Press, San Diego, 1996.

[2] M. S. Dresselhaus, G. Dresselhaus, and P. Avouris, *Carbon Nanotubes*. Springer-Verlag, Berlin, 1996.

[3] S. Iijima, Helical microtubules of Graphitic Carbon. *Nature (London)* **354**, 56 (1991).

[4] H. W. Kroto, J. R. Heath, S. C. O'Brien, R. F. Curl, and R. E. Smalley, C_{60}: Buckminsterfullerene, *Nature (London)* **318**, 162 (1985).

[5] L. Wei, P. K. Kuo, R. L. Thomas, T. R. Anthony, and W. F. Banholzer, Thermal-Conductivity of Isotopically Modified Single-Crystal Diamond, *Phys. Rev. Lett.* **70**(24), 3764 (1993).

[6] R. Saito, G. Dresselhaus, and M. S. Dresselhaus, *Physical Properties of Carbon Nanotubes* (Imperial College Press, London, (1993)).

[7] J. W. Mintmire, B. I. Dunlap, and C. T. White, Are Fullerene Tubules Metallic? *Phys. Rev. Lett.* **68**, 631 (1992).

[8] N. Hamada, S. Sawada, and A. Oshiyama, New One-Dimensional Conductors: Graphitic Microtubules, *Phys. Rev. Lett.* **68**, 1579 (1992).

[9] R. Saito, G. Dresselhaus, and M. S. Dresselhaus, Topological Defects in Large Fullerenes. *Chem. Phys. Lett.* **195**, 537 (1992).

[10] R. A. Jishi, L. Venkataraman, M. S. Dresselhaus, and G. Dresselhaus, Phonon Modes in Carbon Nanotubules, *Chem. Phys. Lett.* **209**, 77 (1993).

[11] M. S. Dresslehaus and P. C. Eklund, Phonons in Carbon Nanotubes, *Adv. Phys.* **49**(6), 705–814 (2000).

[12] C. Oshima, T. Aizawa, R. Souda, Y. Ishizawa, and Y. Sumiyoshi, Surface Phonon-Dispersion Curves of Graphite (0001) over the Entire Energy Region, *Solid State Comm.* **65**, 1601 (1988).

[13] T. Aizawa, R. Souda, S. Otani, Y. Ishizawa, and C. Oshima, Bond Softening in Monolayer Graphite Formed on Transition-Metal Carbide Surfaces, *Phys. Rev. B* **42**, 11469 (1990).

[14] L. X. Benedict, S. G. Louie, and M. L. Cohen, Heat Capacity of Carbon Nanotubes. *Solid State Comm.* **100**(3), 177 (1996).

[15] J. Hone, M. Whitney, C. Piskoti, and A. Zettl, Thermal Conductivity of Single-Walled Carbon Nanotubes, *Phys. Rev. B* **59**, R2514 (1999).

[16] P. Kim, L. Shi, A. Majumdar, and P. L. McEuen, Thermal Transport Measurements of Individual Multiwalled Nanotubes, *Phys. Rev. Lett.* **87**, 215502 (2001).

[17] C. Uher, Thermal Conductivity of Graphite, In O. Madelung and G. K. White, eds., *Landolt-Börnstein: Numerical Data and Functional Relationships in Science and Technology* **15c** of *New Series, Group III*, 426–448. Springer-Verlag, Berlin (1991).

[18] P. Jund and R. Jullien, Molecular-Dynamics Calculation of the Thermal Conductivity of Vitreous Silica, *Phys. Rev. B* **59**, 13707 (1999).
[19] M. Schoen and C. Hoheisel, The Shear Viscosity of a Lennard-Jones Fluid Calculated by Equilibrium Molecular-Dynamics, *Mol. Phys.* **56**, 653 (1985).
[20] D. Levesque and L. Verlet, Molecular-Dynamics Calculations of Transport-Coefficients, *Mol. Phys.* **61**, 143 (1987).
[21] D. J. Evans and G. P. Morriss, *Statistical Mechanics of Nonequilibrium Liquids*, Theoretical Chemistry Monograph Series. (Academic Press, London, 1990).
[22] D. A. McQuarrie, *Statistical Mechanics.* (Harper and Row, London, 1976).
[23] J. Che, T. Çağın, and W. A. Goddard III, Thermal Conductivity of Carbon Nanotubes, *Nanotech.* **11**, 65 (2000).
[24] A. Maeda and T. Munakata, Lattice Thermal-Conductivity via Homogeneous Nonequilibrium Molecular-Dynamics, *Phys. Rev. E* **52**, 234 (1995).
[25] D. J. Evans, Homogeneous Nemd Algorithm for Thermal-Conductivity: Application of Non-canonical Linear Response Theory, *Phys. Lett. A* **91**, 457 (1982).
[26] D. P. Hansen and D. J. Evans, A Generalized Heat-Flow Algorithm, *Mol. Phys.* **81**, 767 (1994).
[27] D. C. Rapaport, *The Art of Molecular Dynamics Simulation* (Cambridge University Press, Cambridge, 1998).
[28] S. Nosé, A Molecular-Dynamics Method for Simulations in the Canonical Ensemble, *Mol. Phys.* **52**, 255 (1984).
[29] W. G. Hoover, Canonical Dynamics: Equilibrium Phase-Space Distributions, *Phys. Rev. A* **31**, 1695 (1985).
[30] J. Tersoff, Empirical Interatomic Potential for Carbon, with Applications to Amorphous Carbon, *Phys. Rev. Lett.* **61**, 2879 (1988).
[31] J. Tersoff, New Empirical-Approach for the Structure and Energy of Covalent Systems, *Phys. Rev. B* **37**, 6991 (1988).
[32] Y.-K. Kwon, S. Saito, and D. Tománek, Effect of Intertube Coupling on the Electronic Structure of Carbon Nanotube Ropes, *Phys. Rev. B* **58**, R13314 (1998).
[33] S. Berber, Y.-K. Kwon, and D. Tomanek, Unusually High Thermal Conductivity of Carbon Nanotubes, *Phys. Rev. Lett.* **84**, 4613–16 (2000).
[34] T. R. Anthony, W. F. Banholzer, J. F. Fleischer, L. Wei, P. K. Kuo, R. L. Thomas, and R. W. Pryor, Thermal-Diffusivity of Isotopically Enriched $c_1 2$ Diamond, *Phys. Rev. B* **42**, 1104 (1990).
[35] T. Nihira and T. Iwata, Thermal Resistivity Changes in Electron-Irradiated Pyrolytic-Graphite, *Jpn. J. Appl. Phys.* **14**, 1099 (1975).
[36] M. G. Holland, C. A. Klein, and W. D. Straub, Lorenz Number of Graphite at Very Low Temperatures, *J. Phys. Chem. Solids* **27**, 903 (1966).
[37] A. de Combarieu, Thermic Conductivity of Quasi Monocrystalline Graphite and Effects of Irradiation by Neutrons: 1. Measurements, *J. Phys.-Paris* **28**, 951 (1967).
[38] J. Hone, M. Whitney, and A. Zettl, Thermal Conductivity of Single-Walled Carbon Nanotubes, *Synthetic Metals* **103**, 2498 (1999).
[39] G. W. C. Kaye and T. H. Laby, *Tables of Physical and Chemical Constants*, 16th edition (Longman, London, 1995).
[40] B. T. Kelly, *Physics of Graphite* (Applied Science, London, 1981).

[41] J. Heremans, Jr., and C. P. Beets, Thermal Conductivity and Thermopower of Vapor-Grown Graphite Fibers, *Phys. Rev. B* **32**, 1981 (1985).
[42] R. S. Ruoff and D. C. Lorents, Mechanical and Thermal-Properties of Carbon Nanotubes, *Carbon* **33**, 925 (1995).
[43] W. Yi, L. Lu, Z. Dian-Lin, Z. W. Pan, and S. S. Xie, Linear Specific Heat of Carbon Nanotubes, *Phys. Rev. B* **59**, R9015 (1999).
[44] Z. W. Pan, S. S. Xie, B. H. Chang, C. Y. Wang, L. Lu, W. Liu, W. Y. Ahou, W. Z. Li, and L. X. Quan, Very Long Carbon Nanotubes, *Nature (London)* **394**, 631 (1998).
[45] J. Hone, M. C. Llaguno, N. M. Nemes, A. T. Johnson, J. E. Fischer, D. A. Walters, M. J. Casavant, J. Schmidt, and R. E. Smalley, Electrical and Thermal Transport Properties of Magnetically Aligned Single Walt Carbon Nanotube Films, *Appl. Phys. Lett.* **77**, 666 (2000).
[46] R. Peierls, *Quantum Theory of Solids* (Oxford University Press, Oxford, 1955).
[47] J. Hone, Phonons and Thermal Properties of Carbon Nanotubes, In M. S. Dresselhaus, G. Dresselhaus, and P. Avouris, eds., *Carbon Nanotubes* (Springer-Verlag, Berlin, 2001).
[48] K. Schwab, E. A. Henriksen, J. M. Worlock, and M. L. Roukes, Measurement of the Quantum of Thermal Conductance, *Nature (London)* **404**, 974 (2000).
[49] M. J. Biercuk, M. C. Llaguno, M. Radosavljevic, J. K. Hyun, A. T. Johnson, and J. E. Fischer, Carbon Nanotube Composites for Thermal Management, *Appl. Phys. Lett.* **80**, 2767 (2002).
[50] D. G. Cahill, Thermal-Conductivity Measurement from 30 to 750 K: The 3 ω Method, *Rev. Sci. Instrum.* **61**, 802 (1990).
[51] D. Li, Y. Wu, P. Kim, L. Shi, P. Yang, and A. Majumdar, Thermal Conductivity of Individual Silicon Nanowires, *Appl. Phys. Lett.* **83**, 2934 (2003).
[52] H. Dai, J. H. Hafner, A. G. Rinzler, D. T. Colbert, and R. E. Smalley, Nanotubes as Nanoprobes in Scanning Probe Microscopy, *Nature (London)* **384**, 147 (1996).
[53] L. Shi, P. Kim, P. McEuen, and A. Majumdar, unpublished, 2002.
[54] P. G. Collins, M. Hersam, M. Arnold, R. Martel, and Ph. Avouris, Current Saturation and Electrical Breakdown in multiwalled Carbon Nanotubes, *Phys. Rev. Lett.* **86**, 3128 (2001).